

# The Beijing Climate Center Climate System Model (BCC-CSM): Main Progress from CMIP5 to CMIP6

Tongwen Wu<sup>1\*</sup>, Yixiong Lu<sup>1</sup>, Yongjie Fang<sup>1</sup>, Xiaoge Xin<sup>1</sup>, Laurent Li<sup>1,2</sup>, Weiping Li<sup>1</sup>, Weihua Jie<sup>1</sup>, Jie Zhang<sup>1</sup>, Yiming Liu<sup>1</sup>, Li Zhang<sup>1</sup>, Fang Zhang<sup>1</sup>, Yanwu Zhang<sup>1</sup>, Fanghua Wu<sup>1</sup>, Jianglong Li<sup>1</sup>, Min Chu<sup>1</sup>, Zaizhi Wang<sup>1</sup>, Xueli Shi<sup>1</sup>, Xiangwen Liu<sup>1</sup>, Min Wei<sup>3</sup>, Anning Huang<sup>4</sup>, Yaocun Zhang<sup>4</sup>, Xiaohong Liu<sup>1,5</sup>

<sup>1</sup>Beijing Climate Center, China Meteorological Administration, Beijing, China

<sup>2</sup>Laboratoire de M é t é o r o l o g i e D y n a m i q u e , I P S L , C N R S , S o r b o n n e U n i v e r s i t é E c o l e N o r m a l e S u p é r i e u r e , E c o l e P o l y t e c h n i q u e , P a r i s , F r a n c e

<sup>3</sup>National Meteorological Information Center, China Meteorological Administration, Beijing, China

<sup>4</sup>Nanjing University, Nanjing, China

<sup>5</sup>University of Wyoming, Laramie, WY, United States

*Correspondence to:* Tongwen Wu ([twwu@cma.gov.cn](mailto:twwu@cma.gov.cn))

**(Revised on Feb. 10, 2019)**

**Abstract.** Main progresses of Beijing Climate Center (BCC) climate system model from the phase five of the Coupled Model Intercomparison Project (CMIP5) to its phase six (CMIP6) are presented, in terms of physical parameterizations and model's performance. BCC-CSM1.1 and BCC-CSM1.1m are the two models involved in CMIP5. BCC-CSM2-MR, BCC-CSM2-HR, and BCC-ESM1.0 are the three models configured for CMIP6. Historical simulations from 1851 to 2014 from BCC-CSM2-MR (CMIP6) and from 1851 to 2005 from BCC-CSM1.1m (CMIP5) are used for models assessment. The evaluation matrices include (a) energy budget at top of the atmosphere, (b) surface air temperature, precipitation, and atmospheric circulation for global and East Asia regions, (c) sea surface temperature

28 (SST) in the tropical Pacific, (d) sea ice extent and thickness and Atlantic Meridional Overturning  
29 Circulation (AMOC), and (e) climate variations at different time scales such as global warming trend in  
30 the 20<sup>th</sup> century, stratospheric quasi-biennial oscillation (QBO), Madden-Julian Oscillation (MJO) and  
31 diurnal cycle of precipitation. Compared to BCC-CSM1.1m, BCC-CSM2-MR shows significant  
32 improvements in many aspects including: tropospheric air temperature and circulation at global and  
33 regional scale in East Asia, climate variability at different time scales such as QBO, MJO, diurnal cycle  
34 of precipitation, interannual variations of SST in the equatorial Pacific, and long-term trend of surface  
35 air temperature.

36

## 37 **1. Introduction**

38 Changes of global climate and environment are main challenges that human societies are facing for  
39 sustainable developments. Climate and environment changes are often the consequence of combined  
40 effects of anthropogenic influences and complex interactions among the atmosphere, hydrosphere,  
41 lithosphere, cryosphere and biosphere of the Earth system. To better understand behaviors of the earth  
42 climate, and to predict its future evolution, appropriate new concepts and relevant methodologies should  
43 be proposed and developed. Climate system models are effective tools to simulate the interactions and  
44 feedbacks in an objective manner, and to explore their impacts on climate and climate change. The  
45 Coupled Model Intercomparison Project (CMIP) organized under the auspices of the World Climate  
46 Research Programme's (WCRP) Working Group on Coupled Modelling (WGCM) started twenty years  
47 ago as a comparison of a handful of early global coupled climate models (Meehl et al., 1997). More  
48 than 30 models participated in the phase five of CMIP (CMIP5, Taylor et al., 2012) and created an  
49 unprecedented dynamics in the scientific community to generate climate information and make them  
50 available for scientific researches. Many of these models were then extended into Earth System models  
51 by including the representation of biogeochemical cycles. BCC effectively contributed to CMIP5 by  
52 running most of the mandatory and optional simulations.

53 The first generation of Beijing Climate Center ocean-atmosphere Coupled Model BCC-CM1.0 was  
54 developed from 1995 to 2004 (e.g. Ding et al., 2002). It was mainly used for seasonal climate prediction.  
55 Since 2005, BCC initiated the development of a new fully-coupled climate modelling platform (Wu et

56 al., 2010, 2013, 2014). In 2012, two versions of the BCC model were released: BCC-CSM1.1 with a  
57 coarse horizontal resolution T42 (approximately 280 km) and BCC-CSM1.1m with a medium  
58 horizontal resolution T106 (approximately 110 km). It was a fully-coupled model with ocean, land  
59 surface, atmosphere, and sea-ice components (Wu et al., 2008; Wu, 2012; Xin et al., 2013). Both  
60 versions were extensively used for CMIP5. At the end of 2017, the second generation of the BCC model  
61 was released to run different simulations proposed by the phase six of CMIP (CMIP6, Eyring et al.,  
62 2016). The purpose of this paper is to document the main efforts and progress achieved in BCC for its  
63 climate model transition from CMIP5 to CMIP6. We show improvements in both model resolution and  
64 its physics. A relevant description on model transition, and experiment design are shown in Sections 2  
65 and 3. A comparison of models performance is presented in Section 4. Conclusions and discussion are  
66 summarized in Section 5. Information about code and data availability is shown in Section 6.

## 67 **2. Transition of the BCC climate system model from CMIP5 to CMIP6**

68 Table 1 shows a summary of different BCC models or versions used for CMIP5 and CMIP6. All of  
69 them are fully-coupled global climate models with four components, atmosphere, ocean, land surface  
70 and sea-ice, interacting with each other. They are physically coupled through fluxes of momentum,  
71 energy, water at their interfaces. The coupling was realized with the flux coupler version 5 developed  
72 by the National Center for Atmosphere Research (NCAR). BCC-CSM1.1 and BCC-CSM1.1m are our  
73 two models involved in CMIP5. They differ mainly by their horizontal resolutions. As shown in Table 1,  
74 BCC-CSM2-MR, BCC-CSM2-HR, and BCC-ESM1.0 are the three models developed for CMIP6.

75 BCC-ESM1.0 is our Earth System configuration. It is a global fully-coupled  
76 climate-chemistry-carbon model, and intended to conduct simulations for the Aerosol Chemistry Model  
77 Intercomparison Project (AerChemMIP, Collins et al., 2017) and the Coupled Climate–Carbon Cycle  
78 Model Intercomparison Project (C4MIP, Jones et al., 2016), both endorsed by CMIP6. Its performance  
79 will be presented in a separated paper. BCC-CSM2-HR is our high-resolution configuration prepared  
80 for conducting simulations of the High Resolution Model Intercomparison Project (HighResMIP v1.0,  
81 Haarsma et al., 2016). It has 56 layers in the vertical, 0.092 hPa for the top of model. Its performance  
82 will also be presented separately.

83 In this paper, we focus on BCC-CSM1.1m and BCC-CSM2-MR. The two models are  
84 representative of our climate modelling efforts in CMIP5 and CMIP6 respectively. They have the same  
85 horizontal resolution (T106, about 110×110 km in the atmosphere and 30×30 km in the tropical ocean),  
86 ensuring a fair comparison. But they have different vertical resolutions in the atmosphere (Table 1),  
87 which are 26 layers with its top at 2.917 hPa in BCC-CSM1.1m and 46 layers with its top at 1.459 hPa  
88 in BCC-CSM2-MR (Figure 1). The present version of BCC-CSM2-MR takes 50% more computing  
89 time than BCC-CSM1.1m for the same amount of parallel computing processors.

## 90 **2.1 Atmospheric component BCC-AGCM**

91 The atmospheric component of BCC-CSM1.1m is BCC-AGCM2.2 (second generation). It is  
92 detailed in a series of publications (Wu et al., 2008, 2010; Wu, 2012; Wu et al., 2013).  
93 BCC-AGCM3-MR is its updated version (third generation), used as the atmosphere component in  
94 BCC-CSM2-MR. The dynamic core in the two models is identical and uses the spectral framework  
95 described in Wu et al. (2008), in which a reference stratified atmospheric temperature and a reference  
96 surface pressure are introduced into the governing equations to improve pressure gradient force and  
97 gradients of surface pressure and temperature, the prognostic variables for temperature and surface  
98 pressure are separately replaced by their perturbations from their references. Explicit time difference  
99 scheme is applied to vorticity equation, and semi-implicit time difference scheme for divergence,  
100 temperature, and surface pressure equations. Semi-Lagrangian tracer transport scheme is used for water  
101 vapor, liquid cloud water and ice cloud water. Main differences of model physics used in the two  
102 models (BCC-AGCM2.2 and BCC-AGCM3-MR) are summarized in Table 2 and details in the  
103 following:

### 104 ***a. Deep convection***

105 Our second-generation atmospheric model, BCC-AGCM2.2, operates with a parameterization  
106 scheme of deep cumulus convection developed by Wu (2012). Main characteristics can be summarized  
107 as follows:

108 (1) Deep convection is initiated at the level of maximum moist static energy above the boundary  
109 layer. It is triggered when there is positive convective available potential energy (CAPE) and if the  
110 relative humidity of the air at the lifting level of convective cloud is greater than 75%;

111 (2) A bulk cloud model taking into account processes of entrainment/detrainment is used to  
112 calculate the convective updraft with consideration of budgets for mass, dry static energy, moisture,  
113 cloud liquid water, and momentum. The scheme also considers the lateral entrainment of the  
114 environmental air into the unstable ascending parcel before it rises to the lifting condensation level. The  
115 entrainment/detrainment amount for the updraft cloud parcel is determined according to the  
116 increase/decrease of updraft parcel mass with altitude. Based on a total energy conservation equation of  
117 the whole adiabatic system involving the updraft cloud parcel and the environment, the mass change for  
118 the adiabatic ascent of the cloud parcel with altitude is derived;

119 (3) The convective downdraft is assumed to be saturated and originated from the level of minimum  
120 environmental saturated equivalent potential temperature within the updraft cloud;

121 (4) The closure scheme determining the mass flux at the base of convective cloud is that suggested  
122 by Zhang (2002). It assumes that the increase/decrease of CAPE due to changes of the thermodynamic  
123 states in the free troposphere resulting from convection approximately balances the decrease/increase  
124 resulting from large-scale processes.

125 A modified version of Wu (2012) is used in BCC-AGCM3-MR for deep convection  
126 parameterization. The convection is triggered only when the boundary layer is unstable or there exists  
127 updraft velocity in the environment at the lifting level of convective cloud, and simultaneously there is  
128 positive CAPE. This modification is aimed to connect the deep convection to the instability of the  
129 boundary layer. The lifting condensation level is set to above the nominal level of non-divergence (600  
130 hPa) in BCC-AGCM2.2 and lowered to the level of 650 hPa in BCC-AGCM3-MR. These modifications  
131 in the deep convection scheme are found to improve the simulation of diurnal cycle of precipitation and  
132 Madden-Julian Oscillation (MJO).

### 133 ***b. Shallow convection***

134 Shallow convection is parameterized with a local convective transport scheme (Hack, 1994). It is  
135 used to remove any local instability that may remain after the deep convection scheme. This Hack  
136 convection scheme is largely-used one to typically represent shallow subtropical convection and  
137 midlevel convection that do not originate from the boundary layer.

### 138 ***c. Cloud macrophysics***

139 Cloud macrophysics comprises physical processes to compute cloud fractions in each layer,  
 140 horizontal and vertical overlapping of clouds, and conversion rates of water vapor into cloud  
 141 condensates. In BCC-AGCM2.2, cloud fraction and the associated cloud macrophysics follow what  
 142 designed in NCAR Community Atmosphere Model version 3 (CAM3, Collins et al., 2004). The total  
 143 cloud cover ( $C_{tot}$ ) within each model grid is set as the maximum value of three cloud covers: low-level  
 144 marine stratus ( $C_{mst}$ ), convective cloud ( $C_{conv}$ ), and stratus cloud ( $C_s$ ),

$$145 \quad C_{tot} = \max(C_{conv}, C_{mst}, C_s) \quad (1)$$

146 As in CAM3, the marine stratocumulus cloud is diagnosed with an empirical relationship between the  
 147 cloud fraction and the boundary layer stratification which is evaluated with atmospheric variables at  
 148 surface and 700mb (Klein and Hartmann, 1993). The convective cloud fraction uses a functional form  
 149 of Xu and Krueger (1991) relating the cloud cover to updraft mass flux from the deep and shallow  
 150 convection schemes. The stratus cloud fraction is diagnosed on the basis of relative humidity which  
 151 varies with pressure.

152 A new cloud scheme is developed and used in BCC-AGCM3-MR. It consists of calculating  
 153 convective cloud and the total cloud cover in a different way from BCC-AGCM2.2. The total cloud  
 154 fraction in each model grid cell is given as

$$155 \quad C_{tot} = C_{conv} + (1 - C_{conv}) \max(C_{mst}, C_s) \quad (2)$$

156 And the convective cloud  $C_{conv}$  is assumed to be the sum of shallow ( $C_{shallow}$ ) and deep ( $C_{deep}$ )  
 157 convective cloud fractions:

$$158 \quad C_{conv} = C_{shallow} + C_{deep} \quad (3)$$

159  $C_{shallow}$  and  $C_{deep}$  are non-overlapped with each other and diagnosed following the relationships,

$$160 \quad C_{conv} q^*(T_c) + (1 - C_{conv}) \bar{q} = \bar{q}_{conv} \quad (4)$$

$$161 \quad C_{conv} T_c + (1 - C_{conv}) \bar{T} = \bar{T}_{conv} \quad (5)$$

162 and

$$163 \quad q^*(T_c) = q^*(\bar{T}) + \frac{\partial q^*(\bar{T})}{\partial \bar{T}} (T_c - \bar{T}) \quad (6)$$

164 where  $\bar{q}$  and  $\bar{T}$ ,  $\bar{q}_{conv}$  and  $\bar{T}_{conv}$  denote the model grid box-averaged water vapor mixing ratio and  
 165 temperature in the ‘environment’ before and after convection activity, respectively.  $T_c$  and  $q^*(T_c)$  are  
 166 the temperature inside the convective cloud plume and its saturated water vapor mixing ratio. Here, we  
 167 assume that the shallow and deep convection can concurrently occur in the same atmospheric column at  
 168 any time step. That is, the shallow convection scheme follows the deep convection and occurs at  
 169 vertical layers where local instability still remains after deep convection.

170 If no supersaturation exists in clouds, we can obtain from Eqs. (4) and (5)

$$171 \quad C_{conv} = \frac{(\bar{q}_{conv} - \bar{q}) - \frac{\partial q^*(\bar{T})}{\partial \bar{T}}(\bar{T}_{conv} - \bar{T})}{q^*(\bar{T}) - \bar{q}}. \quad (7)$$

172 The temperature  $T_c$  and the specific humidity  $q_c = q^*(T_c)$  of the cloud plume can be firstly derived  
 173 from Eqs. (5) and (6). Following the method above, the cloud fraction ( $C_{deep}$  and  $C_{shallow}$ ),  
 174 temperature ( $T_{deep}$  and  $T_{shallow}$ ), specific humidity ( $q_{deep}$  and  $q_{shallow}$ ) for the deep convective,  
 175 shallow convective clouds can be then deduced sequentially.

176 After the three moisture processes (i.e. deep convection, then shallow convection, and finally  
 177 stratiform precipitation) are finished, the mean temperature ( $\bar{T}_{box}$ ) and specific humidity ( $\bar{q}_{box}$ ) of the  
 178 whole model-grid box are then updated. Ambient temperature ( $\bar{T}_{ambient}$ ) and specific humidity  
 179 ( $\bar{q}_{ambient}$ ) outside convective clouds can be finally estimated using the following Eqs.,

$$180 \quad \bar{q}_{box} = \bar{q}_{ambient} \cdot (1 - C_{deep} - C_{shallow}) + q_{deep} \cdot C_{deep} + q_{shallow} \cdot C_{shallow}, \quad (8)$$

181 and

$$182 \quad \bar{T}_{box} = \bar{T}_{ambient} \cdot (1 - C_{deep} - C_{shallow}) + T_{deep} \cdot C_{deep} + T_{shallow} \cdot C_{shallow}. \quad (9)$$

183 Finally, the stratus cloud fraction  $C_s$  is diagnosed on the basis of the relative humidity ( $RH_{ambient}$ ) of  
 184 the ambient,

$$185 \quad C_s = \left( \frac{RH_{ambient} - RH_{min}}{1 - RH_{min}} \right)^2 \quad (10)$$

186 where  $RH_{min}$  is a threshold of relative humidity and  $RH_{ambient}$  is derived with  $\bar{T}_{ambient}$  and  $\bar{q}_{ambient}$ .  
 187 If  $C_{deep} + C_{shallow} > 1$  in Eqs. (8) and (9),  $C_{deep}$  and  $C_{shallow}$  are scaled to meet the condition  
 188  $C_{deep} + C_{shallow} = 1.0$ , and then  $C_s = 0$ . At that condition, we do not calculate  $\bar{T}_{ambient}$  and  
 189  $\bar{q}_{ambient}$  from Eqs. (8) and (9).

#### 190 **d. Cloud microphysics**

191 In BCC-AGCM2.2 and BCC-AGCM3-MR, the essential part of the stratiform cloud microphysics  
 192 remains the same and follows the framework of non-convective cloud processes in CAM 3.0 (Collins et  
 193 al., 2004) that is the scheme proposed by Rasch and Kristj ánsson (1998) and modified by Zhang et al.  
 194 (2003). However there is a noticeable difference of cloud microphysics in the two models concerning  
 195 the treatments for indirect effects of aerosols through mechanisms of clouds and precipitation. Indirect  
 196 effects of aerosols were not included in BCC-AGCM2.2 for CMIP5. That is, the cloud droplets  
 197 effective radius was not related to aerosols, neither the precipitation efficiency. The cloud droplets  
 198 effective radius was either prescribed or a simple function of atmospheric temperature. The effective  
 199 radius for warm clouds was specified to be  $14 \mu\text{m}$  over open ocean and sea ice, and was a function of  
 200 atmospheric temperature over land. For ice clouds, the effective radius was also a function of  
 201 temperature following Kristj ánsson et al. (2000).

202 Aerosol particles influence clouds and the hydrological cycle by their ability to act as cloud  
 203 condensation nuclei and ice nuclei. This indirect radiative forcing of aerosols is included in the latest  
 204 version of BCC-AGCM3-MR, with the effective radius of liquid water cloud droplets being related to  
 205 the cloud droplet number concentration  $N_{cdnc}$  ( $\text{cm}^{-3}$ ). As proposed by Martin et al. (1994), the  
 206 volume-weighted mean cloud droplet radius  $r_{i,vol}$  can be expressed as

$$207 \quad r_{i,vol} = \left[ (3LWC) / (4\pi\rho_w N_{cdnc}) \right]^{1/3}, \quad (11)$$

208 where  $\rho_w$  is the liquid water density, LWC is the cloud liquid water content ( $\text{g cm}^{-3}$ ). Cloud water  
 209 and ice contents are prognostic variables in our model with source and sink terms taking into account  
 210 the cloud microphysics. The effective radius of cloud droplets  $r_{el}$  is then estimated as

$$211 \quad r_{el} = \beta \cdot r_{i,vol} \quad (12)$$



212 where  $\beta$  is a parameter dependent on the droplets spectral shape. There are various methods to  
 213 parameterize it (e.g. Pontikis and Hicks, 1992; Liu and Daum, 2002). We use the calculation proposed  
 214 by Peng and Lohmann (2003),

$$215 \quad \beta = 0.00084N_{cdnc} + 1.22 \quad (13)$$

216 In BCC-AGCM3-MR, the liquid cloud droplet number concentration  $N_{cdnc}$  ( $\text{cm}^{-3}$ ) is a diagnostic  
 217 variable dependent on aerosols mass. It is explicitly calculated with the empirical function suggested by  
 218 Boucher and Lohmann (1995) and Quaas et al. (2006) :

$$219 \quad N_{cdnc} = \exp[5.1 + 0.41 \ln(m_{aero})] \quad (14)$$

220 The total aerosols mass is the sum of four types of aerosol,

$$221 \quad m_{aero} = m_{SS} + m_{OC} + m_{SO_4} + m_{NH_4NO_2} \cdot \quad (15)$$

222 Here,  $m_{aero}$  ( $\mu\text{g}\cdot\text{m}^{-3}$ ) is the total mass of all hydrophilic aerosols, i.e., the first bin (0.2 to 0.5  $\mu\text{m}$ ) of  
 223 sea salt ( $m_{SS}$ ), hydrophilic organic carbon ( $m_{OC}$ ), sulphate ( $m_{SO_4}$ ), and nitrate ( $m_{NH_4NO_4}$ ). Nitrate as a  
 224 rapidly increasing aerosol species in recent years affects present climate and potentially has large  
 225 implications on climate change (Xu and Penner, 2012; Li et al., 2014). A dataset of nitrate from NCAR  
 226 CAM-Chem (Lamarque et al., 2012) is used in our model.

227 Aerosols also exert impacts on precipitation efficiency (Albrecht, 1989), which is taken into  
 228 account in the parameterization of non-convective cloud processes. We use the same scheme as in  
 229 CAM3 (Rasch and Kristjánsson, 1998; Zhang et al., 2003). There are five processes that convert  
 230 condensate to precipitate: auto-conversion of liquid water to rain, collection of cloud water by rain,  
 231 auto-conversion of ice to snow, collection of ice by snow, and collection of liquid by snow. The  
 232 auto-conversion of cloud liquid water to rain (PWAUT) is dependent on the cloud droplet number  
 233 concentration and follows a formula that was originally suggested by Chen and Cotton [1987],

$$234 \quad PWAUT = C_{l,aut} \hat{q}_1^2 \rho_a / \rho_w \left( \frac{q_l \rho_a}{\rho_w N_{cdnc}} \right)^{1/3} H(r_{l,vol} - r_{ic,vol}) \quad (16)$$

235 Where  $\hat{q}_1$  is in-cloud liquid water mixing ratio,  $\rho_a$  and  $\rho_w$  are the local densities of air and water  
 236 respectively, and

237 
$$C_{l,aut} = 0.55\pi^{1/3} k (3/4)^{4/3} (1.1)^4 . \quad (17)$$

238 In which  $k = 1.18 \times 10^6 \text{ cm}^{-1} \text{ sec}^{-1}$  is the Stokes constant.  $H(x)$  is the Heaviside step function with  
 239 the definition,

240 
$$H(x) = \begin{cases} 0, & x < 0 \\ 1, & x \geq 0 \end{cases} \quad (18)$$

241  $r_{lc,vol}$  is the critical value of mean volume radius of the liquid cloud droplets  $r_{l,vol}$ , and set to  $15 \mu \text{ m}$ .

242 ***e. Gravity wave drag***

243 Gravity waves can be generated by a variety of sources including orography, convection, and  
 244 geostrophic adjustment in regions of baroclinic instability (Richter et al., 2010). Gravity waves  
 245 propagate upward from their source regions and break when large amplitudes are attained. This  
 246 produces a drag on the mean flow. Gravity wave drag plays an important role in explaining the zonal  
 247 mean flow and thermal structure in the upper atmosphere.

248 In previous versions of BCC models, the orographic gravity wave drag was parameterized as in  
 249 McFarlane (1987), but non-orographic sources such as convection and jet-front systems were not  
 250 considered. In BCC-AGCM3-MR, the gravity wave drag generated from convective sources is  
 251 introduced as in Beres et al. (2004), but drag by frontal gravity waves and orographic blocking effects  
 252 are still not involved. The key point of the Beres' scheme is relating the momentum flux phase speed  
 253 spectrum to the convective heating properties. In the present version of BCC-AGCM3-MR, the  
 254 convective gravity wave parameterization is activated only when the deep convective heating depth is  
 255 greater than 2.5 km. Gravity waves generated by topography and fronts are important for higher  
 256 latitudes. The efficiency parameter in the McFarlane scheme is set to 0.125 in BCC-AGCM2.2 and  
 257 doubled to 0.25 in BCC-AGCM3-MR to obtain a better result of the polar night jet. In future, it is  
 258 planned to improve the orographic gravity wave scheme and to implement parameterizations of gravity  
 259 waves emitted by fronts and jets.

260 In the convective gravity wave scheme, the uncertainty in the magnitude of momentum flux arises  
 261 from the horizontal scale of the heating and the convective fraction. The convective fraction (CF) within  
 262 a grid cell is an important parameter and can be tuned to obtain right wave amplitudes. It is a constant

263 and valid for all latitudes where convection is active. Previous studies of Alexander et al. (2004) show  
 264 that CF can vary from ~0.2% to ~7%–8%. We use 5% in BCC-AGCM3-MR. This parameterization  
 265 scheme of convective gravity waves can improve the model’s ability to simulate the stratospheric  
 266 quasi-biennial oscillation in BCC-AGCM3-MR.

267 ***f. Radiative transfer***

268 The radiative transfer parameterization in BCC-AGCM2.2 follows the scheme initially  
 269 implemented in CAM3 (Collins et al., 2004). Aerosol indirect effects on radiation are not taken into  
 270 account and cloud droplets effective radius is only function of temperature for cold clouds and  
 271 prescribed to different values for maritime, polar, and continental cases for warm clouds. In  
 272 BCC-AGCM3-MR, however, the aerosol indirect effects are fully included and the effective radius of  
 273 droplets for liquid clouds is calculated by Equation (12) using the liquid cloud droplet number  
 274 concentration.

275 ***g. Boundary layer turbulence***

276 BCC-AGCM3-MR basically inherits the boundary layer turbulence parameterization used in  
 277 BCC-AGCM2.2, which is based on the eddy diffusivity approach (Holtslag and Boville, 1993). The  
 278 eddy diffusivity is given by

279 
$$K_c = kw_t z \left(1 - \frac{z}{h}\right)^2, \quad (19)$$

280 where  $w_t$  is a turbulent velocity and  $h$  is the boundary layer height, which is estimated as

281 
$$h = z_s + \frac{Ri_c \left\{ [u(h) - u_{SL}]^2 + [v(h) - v_{SL}]^2 + \beta u_*^2 \right\}}{(g/\theta_{SL}) [\theta_v(h) - \theta_{SL}]}, \quad (20)$$

282 where  $z_s$  is the height of the lowest model level,  $u$ ,  $v$ , and  $\theta_v$  are horizontal wind components and  
 283 virtual potential temperature at height  $z$ ,  $u_{SL}$ ,  $v_{SL}$ , and  $\theta_{SL}$  represent the same variables, but in the  
 284 surface layer.  $\beta$  in Eq. (20) is a constant and taken as 100.  $u_*$  is the friction velocity, and  $g$  is  
 285 gravitational acceleration.

286 The critical Richardson number  $Ri_c$  in Eq. (20) is a key parameter for calculating the boundary layer  
 287 height and is set to a constant (0.3) for all stable conditions in BCC-AGCM2.2. In BCC-AGCM3-MR,

288  $Ri_c$  varies according to conditions of boundary layer stability to yield more accurate estimates of  
289 boundary layer height, and set to 0.24 for strongly stable conditions, 0.31 for weakly stable conditions,  
290 and 0.39 for unstable conditions based on observational studies of Zhang et al. (2014).

## 291 **2.2 Land component BCC-AVIM**

292 BCC-AVIM, Beijing Climate Center Atmosphere-Vegetation Interaction Model, is a  
293 comprehensive land surface scheme developed and maintained in BCC. The version 1 (BCC-AVIM1.0)  
294 was used as the land component in BCC-CSM1.1m participating in CMIP5 (Wu et al., 2013). It  
295 includes major land surface biophysical and plant physiological processes. Its origin could go back to  
296 the Atmosphere-Vegetation Interaction Model (AVIM) (Ji, 1995; Ji et al., 2008) with the necessary  
297 framework to include biophysical, physiological, and soil carbon-nitrogen dynamical processes. The  
298 biophysical module in BCC-AVIM1.0, with 10 layers for soil and up to five layers for snow, is almost  
299 the same as that used in the NCAR Community Land Model version 3 (CLM3) (Oleson et al., 2004).  
300 The terrestrial carbon cycle in BCC-AVIM1.0 consists of a series of biochemical and physiological  
301 processes modulating photosynthesis and respiration of vegetation. Carbon assimilated by vegetation is  
302 parameterized by a seasonally varying allocation of carbohydrate to leaves, stem, and root tissues as a  
303 function of the prognostic leaf area index. Litter due to turnover and mortality of vegetation, and carbon  
304 dioxide release into atmosphere through the heterogeneous respiration of soil microbes is taken into  
305 account in BCC-AVIM1.0. Vegetation litter falls to the ground surface and into the soil is divided into  
306 eight idealized terrestrial carbon pools according to the timescale of carbon decomposition of each pool  
307 and transfers among different pools, which is similar to that in the carbon exchange between vegetation,  
308 soil and the atmosphere (CEVSA) model (Cao and Woodward, 1998).

309 BCC-AVIM1.0 has been updated to BCC-AVIM2.0 which serves as the land component of  
310 BCC-CSM2-MR participating in CMIP6. As listed in Table 3, several improvements have been  
311 implemented in BCC-AVIM2.0, such as the inclusion of a variable temperature threshold to determine  
312 soil water freezing/thawing rather than fixed at 0°C, a better calculation of snow surface albedo and  
313 snow cover fraction, a dynamic phenology for deciduous plant function types, and a four-stream  
314 approximation on solar radiation transfer through vegetation canopy. Besides, a simple scheme for  
315 surface fluxes over rice paddy is also implemented in BCC-AVIM2.0. These improvements are briefly

316 discussed as follows.

317 (a) Soil water freezes at the constant temperature 0 °C in BCC-AVIM1.0, but the actual  
318 freezing-thawing process is a slowly and continuously changing process. We take into account the fact  
319 that the soil water potential remains in equilibrium with the water vapor pressure over pure ice when  
320 soil ice is present. Based on the relationships among soil water matrix potential  $\psi$  (mm), soil  
321 temperature and soil water content, a variable temperature threshold for freeze-thaw dependent on soil  
322 liquid water content, soil porosity and saturated soil matrix potential is introduced. The inclusion of this  
323 scheme improves the performance of BCC-AVIM2.0 in the simulation about seasonal frozen soil (Xia et  
324 al., 2011).

325 (b) In BCC-AVIM1.0, we took into account the snow aging effect on surface albedo with a simple  
326 consideration by using a unified scheme to mimic the snow surface albedo decrease with time. In  
327 BCC-AVIM2.0, we assume different reduction rates of snow albedo with actual elapsed time after  
328 snowfalls in the accumulating and melting stages of a snow season (Chen et al., 2014). Besides, the  
329 variability of sub-grid topography is now taken into account to calculate the snow cover fraction within  
330 a model grid cell.

331 (c) Unlike the empirical plant leaf unfolding and withering dates prescribed in BCC-AVIM1.0, a  
332 dynamic determination of leaf unfolding, growth, and withering dates according to the budget of  
333 photosynthetic assimilation of carbon similar to the phenology scheme in CTEM (Arora, 2005) was  
334 implemented in BCC-AVIM2.0. Leaf loss due to drought and cold stresses in addition to natural  
335 turnover are also considered.

336 (d) The four-stream solar radiation transfer scheme within canopy in BCC-AVIM2.0 is based on  
337 the same radiative transfer theory used in atmosphere (Liou, 2004). It adopts the analytic formula of  
338 Henyey-Greenstein for the phase function. The vertical distribution of diffuse light within canopy is  
339 related to transmissivity and reflectivity of leaves, besides, average leaf angle and direction of incident  
340 direct beam radiation influence diffuse light within canopy as well. The upward and downward radiative  
341 fluxes are determined by the phase function of diffuse light, G-function, leaf reflectivity and  
342 transmissivity, leaf area index, and the cosine of solar angle of incident direct beam radiation (Zhou et al.,  
343 2018).

344 (e) Considering the wide distribution of rice paddies in Southeast Asia and the quite different  
345 characteristics of rice paddies and bare soil, a scheme to parameterize the surface albedo, roughness  
346 length, turbulent sensible and latent heat fluxes over rice paddies is developed (a manuscript is in  
347 preparation) and implemented in BCC-AVIM2.0.

348 (f) Finally, land-use and land-cover changes are explicitly involved in BCC-AVIM2.0. An increase  
349 in crop area implies the replacement of natural vegetation by crops, which is often known as  
350 deforestation.

### 351 **2.3 Ocean and Sea Ice**

352 There are no significant changes for the ocean and sea ice from BCC-CSM1.1m to  
353 BCC-CSM2-MR. But for the sake of completeness, we present here a short description of them. The  
354 oceanic component is MOM4-L40, an oceanic GCM. It was based on the Z-coordinate Modular Ocean  
355 Model (MOM), version 4 (Griffies, 2005) developed by the Geophysical Fluid Dynamics Laboratory  
356 (GFDL). It has a nominal resolution of  $1^\circ \times 1^\circ$  with a tri-pole grid, the actual resolution being from  $1/3^\circ$   
357 latitude between  $30^\circ \text{S}$  and  $30^\circ \text{N}$  to  $1.0^\circ$  at  $60^\circ$  latitude. There are 40 z-levels in the vertical. The two  
358 northern poles of the curvilinear grid are distributed to land areas over Northern America and over the  
359 Eurasian continent. There are 13 vertical levels placed between the surface and the 300-m depth of the  
360 upper ocean. MOM4\_L40 adopts some mature parameterization schemes, including Swedy's  
361 tracer-based third order advection scheme, isopycnal tracer mixing and diffusion scheme (Gent and  
362 McWilliams, 1990), Laplace horizontal friction scheme, KPP vertical mixing scheme (Large et al.,  
363 1994), complete convection scheme (Rahmstorf, 1993), overflow scheme of topographic processing of  
364 sea bottom boundary/steep slopes (Campin & Goosse, 1999), and shortwave penetration schemes based  
365 on spatial distribution of chlorophyll concentration (Sweeney et al., 2005).

366 Concentration and thickness of sea ice are calculated by the Sea Ice Simulator (SIS) developed by  
367 GFDL (Winton, 2000). It is a global sea ice thermodynamic model including the Elastic-Viscous-  
368 Plastic dynamic process and Semtner's thermodynamic process. SIS has 3 vertical layers, including 1  
369 snow cover and 2 ice layers of equal thickness. In each grid, 5 categories of sea ice (including open  
370 water) are considered, according to the thickness of sea ice. It also takes into account the mutual  
371 transformation from one category to another under thermodynamic conditions. The sea ice model

operates on the same oceanic grid and has the same horizontal resolution of MOM\_L40. SIS calculates concentration, thickness, temperature, salinity of sea ice and motions of snow cover and ice sheet. There is no gas exchange through sea ice.

#### 2.4. Surface turbulent fluxes between air and sea/sea ice

The atmosphere and sea/sea ice interplay through the exchange of surface turbulent fluxes of momentum, heat and water. An optimum treatment of the surface exchange, sound in physics and economic in computation, is very important in simulating the climate variability. During the past years, we maintain a continuous effort to improve the turbulent exchange processes between air and sea/sea ice in different versions of BCC models.

In BCC-CSM1.1m, the bulk formulas of turbulent fluxes over sea surface originate from those used in CAM3, with some modifications to the roughness lengths and corrections to the temperature and moisture gradients considering sea spray effects (Wu et al., 2010). The bulk formulas are updated in BCC-CSM2-MR. The coefficients in roughness lengths calculations were adjusted and the arbitrary gradient corrections are not used. Instead, a gustiness parameterization is included to account for the subgrid wind variability that is contributed by boundary layer eddies, convective precipitation, and cloudiness (Zeng et al., 2002).

In terms of turbulent exchange between air and sea ice, we proposed a new bulk algorithm aiming to improve flux parameterizations over sea ice (Lu et al., 2013). Based on theoretical and observational analysis, the new algorithm employs superior stability functions for stable stratification as suggested by Zeng et al. (1998), and features varying roughness lengths. All the three roughness lengths ( $z_0$ ,  $z_T$ ,  $z_Q$ ) of sea ice were set to a constant (0.5 mm) in BCC-CSM1.1m. Observational studies show that values of  $z_0$  tend to be smaller than 0.5 mm over sea ice in winter and larger than 0.5 mm in summer (Andreas et al., 2010a; Andreas et al., 2010b). In the new parameterization used in BCC-CSM2-MR, the roughness lengths for momentum differentiate between warm and cold seasons. For simplicity,  $z_0$  is treated as

$$z_0(mm) = \begin{cases} 0.1 & \text{for } T_s \leq -2^\circ C \\ 0.8 & \text{for } T_s > -2^\circ C \end{cases}, \quad (19)$$

where  $T_s$  represents surface temperature. For the scalar roughness lengths, a theoretical-based model proposed by Andreas (1987) is used in the new scheme. This model expresses the scalar roughness  $z_s$

399 ( $z_T$  or  $z_Q$ ) as a function of the roughness Reynolds number  $R^*$ , i.e.,

$$400 \quad \ln(z_s/z_0) = b_0 + b_1(\ln R^*) + b_2(\ln R^*)^2. \quad (20)$$

401 Andreas (1987, 2002) tabulates the polynomial coefficients  $b_0$ ,  $b_1$  and  $b_2$ .

### 402 **3. Experimental design**

403 All BCC simulations presented in this work follow the protocols defined by CMIP5 and CMIP6.  
404 We pay attention for them to be comparable in spite of showing the transition of our climate system  
405 model from CMIP5 to CMIP6. The principal simulation to be analyzed is the historical simulation  
406 (hereafter historical) with prescribed forcings from 1850 to 2005 for CMIP5 (to 2014 for CMIP6).

407 Historical forcings data are based as far as possible on observations and downloaded from the  
408 webpage (<https://esgf-node.llnl.gov/search/input4mips/>). They mainly include: (1) GHG concentrations  
409 (only CO<sub>2</sub>, N<sub>2</sub>O, CH<sub>4</sub>, CFC11, CFC12 used in BCC models) with zonal-mean values and updated  
410 monthly; (2) Yearly global gridded land-use forcing; (3) Solar forcing; (4) Stratospheric aerosols (from  
411 volcanoes); (5) CMIP6-recommended anthropogenic aerosol optical properties which is formulated in  
412 terms of nine spatial plumes associated with different major anthropogenic source regions (Stevens et  
413 al., 2017). (6) Time-varying gridded ozone concentrations. In addition, aerosol masses based on CMIP5  
414 (Taylor et al., 2012) are used for on-line calculation of cloud droplet effective radius in BCC model.

415 The preindustrial initial state of BCC-CSM2-MR is preceded by a 500-years piControl simulation  
416 following the requirement of CMIP6. The initial state of the piControl simulation itself is obtained  
417 through individual spin-up runs of each component of BCC-CSM2-MR in order for piControl  
418 simulation to run stably and fast to its model equilibrium. Actually, the initial states of atmosphere and  
419 land are obtained from a 10-years AMIP run forced with monthly climatology of sea surface  
420 temperature (SST) and sea ice concentration, and the initial states of ocean and sea ice are derived from  
421 a 1000-years forced run with a repeating annual cycle of monthly climatology of atmospheric state from  
422 the Coordinated Ocean-Ice Reference Experiment (CORE) dataset version 2 (Danabasoglu et al., 2014).  
423 Figure 2 shows time series of the annual and global mean of net energy flux at top of the atmosphere  
424 (TOA) and the sea surface temperature for 600 years in the piControl simulation. The whole system in  
425 BCC-CSM2-MR fluctuates around  $+0.4 \text{ W m}^{-2}$  net energy flux at TOA without obvious trend in 600  
426 years. The global mean surface air temperature shows a small warming after 600 years (Fig. 2b). During



427 the last 300 years, there are ( $\pm 0.2$  K amplitude) oscillations of centennial scale for the whole globe and  
428 for the areal average of 60 S to 60 N. They are certainly caused by internal variation of the system.

#### 429 **4. Evaluation and comparison between BCC CMIP5 and CMIP6 models**

##### 430 **4.1 Global Energy Budget**

431 Radiative fluxes at the top of the model atmosphere are fundamental variables characterizing the  
432 Earth's energy balance. Satellite observations in modern time allow us to monitor changes in the net  
433 radiation at top-of-atmosphere (TOA) from 2001 onwards. CERES (Clouds and Earth's Radiant Energy  
434 System) project, with the lessons learned from its predecessor, the Earth's Radiation Budget Experiment  
435 (ERBE), provides improved observation-based data products of Earth's radiation budget (Wielicki et al,  
436 1996). Recently, data of CERES are synthesized with EBAF (Energy Balanced and Filled) data to  
437 derive the CERES-EBAF products, suitable for evaluation of climate models (Loeb et al., 2012). As  
438 shown in Table 4, the TOA shortwave and longwave components in BCC-CSM2-MR are generally  
439 closer to CERES-EBAF compared to those in BCC-CSM1.1m. Model results are for the period 1986–  
440 2005, while the available CERES-EBAF data are for 2003–2014. Globally-averaged TOA net energy is  
441  $0.85 \text{ W m}^{-2}$  in BCC-CSM2-MR and  $0.98 \text{ W m}^{-2}$  in BCC-CSM1.1m for the period from 1986 to 2005.  
442 The energy equilibrium of whole earth system in BCC-CSM2-MR is slightly improved.

443 Clouds constitute a major modulator of the radiative transfer in the atmosphere for both solar and  
444 terrestrial radiations. Their macro and micro properties, including their radiative properties exert strong  
445 impacts on the equilibrium and variation of the radiative budget at TOA or at surface. Figure 3 displays  
446 annual and zonal mean of shortwave, longwave and net cloud radiative forcing for BCC CMIP5 (blue  
447 curves), CMIP6 (red curves) models and observations (black curves). The data used in Fig. 3 are the  
448 same as in Table 4. Although observations and models results cover different time periods, they are still  
449 relevant to reveal climatological mean performance of climate models. In low latitudes between 30 S  
450 and 30 N, BCC-CSM1.1m shows excessive cloud radiative forcing for both shortwave and longwave  
451 radiations. These biases are largely reduced in BCC-CSM2-MR, which is possibly attributed to the new  
452 algorithm of cloud fraction especially for convective cloud amount. Cloud radiative forcing in mid  
453 latitudes shows large uncertainty, also manifested in the large deviation between the two observations.  
454 Cloud radiative forcing in both models is closer to CERES-EBAF than to CERES in mid latitudes. It is

455 clear that the new physics modifies the simulated climate and cloud properties, including the fractional  
456 coverage of clouds, their vertical distribution as well as their liquid water and ice content.

#### 457 **4.2. Performance in Simulating the Global Warming in the 20<sup>th</sup> Century**

458 The historical simulation allows us to evaluate the ability of models to reproduce the global  
459 warming and climate variability in the 20th century. The performance depends on both model  
460 formulation and the time-varying external forcings imposed on the models (Allen et al., 2000). Figure 4  
461 presents global-mean (from 60° S to 60° N) surface air temperature evolutions from HadCRUT4 (Morice  
462 et al., 2012) and BCC CMIP5 and CMIP6 models. Here only the area from 60° S to 60° N is used for  
463 comparison, since few observations existed in polar regions to deduce reliable information in  
464 HadCRUT4, especially before the 20th century. To better reveal long-term trends, the climatological  
465 mean is calculated for the reference period 1961–1990 and removed from the time series. The  
466 interannual variability of both simulations is qualitatively comparable to that observed. When a 11-year  
467 smoothing is applied, the long-term trend of both CMIP6 and CMIP5 models is highly correlated with  
468 HadCRUT4. Figure 4 presents three members of historical simulations from different initial state of the  
469 piControl simulation. The correlation coefficients are 0.90 in CMIP5 and 0.93, 0.93, 0.90 in three  
470 members of CMIP6, respectively.

471 A remarkable feature in Figure 4 is the presence of a global warming hiatus or pause for the period  
472 from 1998 to 2013 when the observed global surface air temperature warming slowed down. This is a  
473 hot topic, largely debated in the scientific research community (e.g. Fyfe et al., 2016; Medhaug et al.,  
474 2017). Two members (r1i1p1f1 and r2i1p1f1 in Fig. 4) of historical simulations of the CMIP6 model  
475 show a hiatus towards the end of the simulation that resembles the observed one. Although the third  
476 member (r3i1p1f1) simulated a global warming slowdown from 2004 to 2012, it is not comparable to  
477 the observed hiatus as it has a short spell of colder years centered at 2010. Another warming hiatus  
478 occurred in the period of 1942 to 1974. The first and the third members (r1i1p1f1 and r3i1p1f1) of  
479 BCC-CSM2-MR only simulate the warming slowdown in the late period from 1958 to 1974, but the  
480 second member (r2i1p1f1) of BCC-CSM2-MR almost simulate this warming hiatus in the whole period  
481 from 1942 to 1974. So, the simulation of global warming hiatus in BCC CMIP6 model clearly excludes  
482 any simple response to forcing, and makes internal variability a much more likely reason.

483 The models response of the SAT to volcanic forcing is slightly stronger than that estimated with  
484 HadCRU data. Evident global cooling shocks are coincident with significant volcanic eruptions such as  
485 Krakatoa (in 1883), West Indies Agung (in 1963), and Mount Pinatubo (in 1991). Each of these  
486 volcanic eruptions significantly enriched stratospheric aerosols (available from  
487 <http://data.giss.nasa.gov/modelforce/strataer/>). As shown in Figure 4, SAT may decrease by up to 0.4 °C  
488 within 1 to 2 years after major volcanic eruptions. The substantial cooling response to volcanic  
489 eruptions is, to a great extent, due to the aerosol direct radiative forcing too strong in both versions of  
490 BCC-CSM.

491 To keep the paper concise and at a reasonable length, only the first member of CMIP6 historical  
492 simulations of BCC-CSM2-MR will be presented hereafter. Biases of annual mean surface air  
493 temperature (at 2 meters) in the whole globe for BCC-CSM2-MR and BCC-CSM1.1m are shown in  
494 Figure 5. In both BCC models, biases are generally within  $\pm 3$  °C, but there are slightly systematic  
495 warm biases over oceans from 50 °S to 50 °N and systematic cold ones over most land regions in north  
496 of 50 °N, in East Asia and in North Africa. Cold biases in high latitudes of the Northern Hemisphere  
497 (North Atlantic, Arctic, North America and Siberia) seem amplified in BCC-CSM2-MR. The land  
498 surface biases in both coupled models are similar to each other. Those patterns of biases are already  
499 present in AMIP simulations (not shown), where effects of oceanic biases are excluded. So those biases  
500 in land surface partly come from their land surface modelling component. In the Southern Ocean, both  
501 models show a strong warm area in the Weddell Sea. BCC-CSM1.1m shows cold biases in other  
502 regions of the Southern Ocean. The disappearance of cold biases in the Southern Oceans in  
503 BCC-CSM2-MR is possibly attributed to the new scheme of cloud fraction (Table 2) as there is a zone  
504 of low-level cloud between 40 °S to 60 °S in the Southern Ocean (omitted), not only in models but also  
505 in observations.

### 506 **4.3 Climate sensitivity to CO<sub>2</sub> increasing**

507 The long trend of global warming in Figure 4 depends on the climate sensitivity which is an  
508 emblematic parameter to characterize the sensitivity of a climate model to external forcing, with all  
509 feedbacks included. It generally designates the variation of global mean surface air temperature in  
510 response to a forcing of doubled CO<sub>2</sub> concentration in the atmosphere (IPCC 2013). As commonly

511 practiced in the climate modelling community, an equilibrium climate sensitivity and a transient climate  
512 response can be separately evaluated, corresponding to a situation of equilibrium and transient states of  
513 climate.

514 We use the standard simulation of 1% CO<sub>2</sub> increase per year (1pctCO<sub>2</sub>) to calculate the transient  
515 climate response (TCR), while the equilibrium climate sensitivity (ECS) uses the 4xCO<sub>2</sub> abrupt-change  
516 simulation by applying the forcing/response regression methodology proposed by Gregory et al. (2004).  
517 The TCR is calculated using the difference of annual surface air temperature between the pre-industrial  
518 experiment and a 20-year period centered on the time of CO<sub>2</sub> doubling in 1pctCO<sub>2</sub>, which is 1.71 for  
519 BCC-CSM2-MR and 2.02 for BCC-CSM1.1m. The ECS is diagnosed from the 150-year run of abrupt  
520 4xCO<sub>2</sub> following the approach of Gregory (2012). The method is based on the linear relationship  
521 (Figure 6) governing the changes of net top-of-atmosphere downward radiative flux and the surface air  
522 temperature simulated in abrupt 4xCO<sub>2</sub> relative to the pre-industrial experiment. The ECS is equal to a  
523 half of the temperature change when the net downward radiative flux reaches zero (Andrews et al.,  
524 2012). It is assumed here that 2xCO<sub>2</sub> forcing is half of that for 4xCO<sub>2</sub>, hypothesis generally verified in  
525 climate models. As shown in Fig. 6, the ECS is 3.03 for BCC-CSM2-MR and 2.89 for BCC-CSM1.1m.  
526 So the TCR of the new version model BCC-CSM2-MR is lower than BCC-CSM1.1m, but the ECS of  
527 BCC-CSM2-MR is slightly higher than BCC-CSM1.1m.

528 The linear regression line shown in Figure 6, as pointed out in Gregory et al. (2012), also allows  
529 estimating the instantaneous forcing due to CO<sub>2</sub> increase, and eventually feedbacks parameter of the  
530 climate system. The former is the cross point of the linear regression line with Y axis: 6.2 W m<sup>-2</sup> for  
531 BCC-CSM2-MR and 7.6 W m<sup>-2</sup> for BCC-CSM1.1m. They can be scaled to the case of 2xCO<sub>2</sub> just with  
532 a division factor of 2. Since ECS values are close to each other in the two models, we can easily deduce  
533 that all-feedback factor is larger in BCC-CSM2-MR than in BCC-CSM1.1m. It is actually not  
534 surprising to see differences of 2xCO<sub>2</sub> radiative forcing between the two models even the radiative  
535 transfer scheme is kept identical, because changes in 3-D structures of cloud, atmospheric temperature  
536 and water vapor do exert impacts on additional radiative forcing due to CO<sub>2</sub> increase in the atmosphere.  
537 It is however interesting to note that feedbacks can operate, in the two models, in such a different way  
538 that ECS keeps almost unchanged between them. We remind that this is a pure coincidence since we did

539 not intentionally tune our model for its sensitivity.

#### 540 **4.4 Behaviors of the atmosphere at present day**

541 The main spatial patterns of observed precipitation climatology are simulated in BCC-CSM1.1m  
542 and BCC-CSM2-MR. Figure 7 shows model biases of annual-mean precipitation for BCC-CSM1.1m  
543 and BCC-CSM2-MR in the globe. They are very close from each other. Their RMSE is also very close:  
544 1.12 mm/day against 1.18 mm/day. Regions of lack of precipitation, such as North India, South China,  
545 the two sides of Sumatra, and the Amazon, experience significant amelioration in the new model.  
546 Excessive rainfalls in Tropical Africa, in the Indian Ocean, in the Maritime Continent seem amplified in  
547 BCC-CSM2-MR. As for the whole globe, the annual mean precipitation coming from convective  
548 process (including deep and shallow convections) accounts for 50% of the total precipitation (2.94  
549 mm/day) in BCC-CSM2-MR and 48% of the total precipitation (2.87 mm/day) in BCC-CSM1.1m. The  
550 convective precipitation increased in BCC-CSM2-MR, and the total amount of precipitation exceeds the  
551 amount (2.68 mm/day) of 1986-2005 mean observed precipitation analyses from Global Precipitation  
552 Climatology Project (Adler et al., 2003). But in some regions such as in the Maritime Continent, stratus  
553 precipitation evidently enhances in BCC-CSM2-MR, where the ratio of convection precipitation to total  
554 precipitation is 39% and even larger than 35% in BCC-CSM1.1m.

555 We now use the Taylor diagram (Figure 8) to evaluate the general performance of our two models  
556 in terms of temperature at 850hPa, precipitation and atmospheric general circulation. The evaluation is  
557 done against climatology of ERA-Interim dataset for the period of 1986 to 2005 (Dee et al., 2011).  
558 ERA-Interim is the latest global atmospheric reanalysis produced by the European Centre for  
559 Medium - Range Weather Forecasts (ECMWF).

560 For global fields, we calculate the spatial pattern correlations between models and ERA-Interim for  
561 the annual-mean climatology of sea level pressure (SLP), temperature at 850 hPa level (T850), zonal  
562 and meridional wind velocity at 850 hPa (U850 and V850), zonal wind velocity at 200 hPa (U200),  
563 geopotential height at 500hPa (Z500), and precipitation from Global Precipitation Climatology Project  
564 (PRCP in Fig. 8, Adler and Chang, 2003) over the period 1980–2000. Except for PRCP and U850  
565 which have lower correlation (less than 0.90) with observation, other variables are all above 0.90 for  
566 their correlation coefficients. The pattern correlation coefficient of Z500 with ERA-Interim is 0.995, the

567 best correlation among these variables. Except for V850, correlations of all other variables in CMIP6  
568 model version (BCC-CSM2-MR) have an evident improvement compared to CMIP5 version  
569 (BCC-CSM1.1m). The normalized standard deviations of most variables except for PRCP and T850 are  
570 obviously improved in BCC-CSM2-MR. As a whole, the performances of most variables in  
571 BCC-CSM2-MR are better than those in BCC-CSM1.1m.

572 Results shown in the Taylor diagrams in Figure 8 about improvements in surface climate and  
573 atmospheric general circulation at different vertical levels are consistent with improvements in the  
574 vertical distribution of atmospheric temperature. Figure 9 shows the yearly-averaged zonal mean of  
575 atmospheric temperature biases in BCC-CSM2-MR and BCC-CSM1.1m, with ERA-Interim for the  
576 period of 1986–2005 as reference. Overall, both BCC-CSM2-MR and BCC-CSM1.1m have similar  
577 biases in their vertical structure, with 1–3 K warmer in the stratosphere (above 100 hPa) for most of the  
578 domain equatorward of 70 °N and 70 °S. There are larger cold biases near the tropopause (centered near  
579 200hPa) for southward of 30 °S and northward of 30 °N. In the middle to lower troposphere (below  
580 400hPa), there is a warm bias of 1-2K. Improvements in BCC-CSM2-MR are mainly located in the  
581 troposphere below 100 hPa. Both cold biases near the tropopause in high latitudes and warm bias in  
582 lower latitudes are reduced.

583 The improvement in tropospheric temperature induces naturally smaller biases for the zonal wind  
584 in the whole troposphere in BCC-CSM2-MR (Figure 9). But there are still westerly wind biases of 6  
585  $\text{m s}^{-1}$  in the layer of 100-200 hPa in the tropics. Westerly jets at mid-latitudes are slightly too strong in  
586 both hemispheres. The zonal mean of zonal wind biases in the high latitudes of the stratosphere in  
587 BCC-CSM2-MR have increased near 10 hPa. The too-strong polar night jets clearly indicate an  
588 insufficient atmospheric drag at this level. It may be partly caused by the lack of effects in relation to  
589 some non-orographic gravity waves generated by atmospheric fronts and jets. We expect to reduce this  
590 model bias in next version by adding this process.

591 Given a much higher vertical resolution and an advanced parameterization of the gravity wave  
592 drag, the new model BCC-CSM2-MR is able to represent the stratospheric quasi-biennial oscillation  
593 (QBO), as shown in Figure 10 which displays time-height diagrams of the tropical zonal winds  
594 averaged from 5 °S to 5 °N. The three panels show observations from the ERA-Interim reanalysis and

595 relevant simulation results from the two models in CMIP6 and CMIP5. Figure 10a shows alternative  
596 westerlies and easterlies in the lower stratosphere appearing with a mean period of about 28 months in  
597 the ERA-Interim reanalysis. In Figure 10b, the BCC-CSM2-MR simulations present a clear  
598 quasi-biennial oscillation of the zonal winds as observed. In this study, the QBO period is taken as the  
599 time between easterly and westerly wind transitions at 20 hPa. The simulation produces about 12 QBO  
600 cycles from 1980 to 2005. The average period is 24.6 months, whereas the shortest and longest cycles  
601 last for 18 and 35 months, respectively. ERA-Interim values are 27.9, 23, and 35 months for average,  
602 minimum, and maximum of cycle length. The observed asymmetry in amplitude with the easterlies  
603 being stronger than the westerlies is reproduced in the simulated zonal winds. At 20 hPa, the simulated  
604 easterlies often exceed  $-20 \text{ m s}^{-1}$ , while in the reanalysis easterly winds peak at  $-30$  to  $-40 \text{ m s}^{-1}$ .  
605 Simulated westerlies of the QBO range from  $8$  to  $12 \text{ m s}^{-1}$ , whereas the reanalysis shows peak winds of  
606  $16$  to  $20 \text{ m s}^{-1}$ . The amplitudes of the QBO cycles in the simulation are weaker than in the reanalysis,  
607 which is possibly due to inadequate gravity wave forcing to drive the QBO. We suspect that the  
608 wave-mean flow interaction based on resolved waves such as Kelvin waves and mixed Rossby-gravity  
609 waves is probably not performant enough in BCC-CSM2-MR. One reason that would contribute to such  
610 a discrepancy is the relatively coarse vertical resolution (Table 1) that would affect the vertical wave  
611 lengths and the wave damping process. The downward propagation of the simulated QBO phases occurs  
612 in a regular manner, but does not penetrate to sufficiently low altitudes. It may depend on the vertical  
613 resolution and the impact of vertical resolution on downward propagation will be discussed in a separate  
614 paper. After a few test of model vertical layers, we tend to conclude that 46 vertical layers (Figure 1)  
615 seem the minimum number to simulate QBO in BCC-CSM2-MR. In BCC-CSM1.1m, however, as  
616 shown in Figure 10c, QBO is inexistent and only a semiannual oscillation of easterlies can be found.

617 Madden-Julian Oscillation (MJO) is a very important atmospheric variability acting within a  
618 periodicity between 20 and 100 days in the tropics with considerable effects on regional weather and  
619 climate. It exerts significant impacts on monsoonal circulations and organization of tropical rainfalls.  
620 From the tropical Indian Ocean to the Western Pacific, MJO shows a pronounced behavior of eastward  
621 propagation, as shown in Figure 11a, in the form of longitude-time, the lagged correlation coefficient of  
622 the rainfall in the eastern Indian Ocean ( $75\text{--}85^\circ \text{E}$ ;  $5^\circ \text{S}\text{--}5^\circ \text{N}$ ) with other positions and with lagged time.

623 We can easily observe the eastward-propagating characteristic, with a moving velocity estimated at 5  
624  $\text{m s}^{-1}$ . As shown in a comparison work of Jiang et al. (2015), three fourth of CMIP5 models don't show  
625 the propagation behavior, with only a standing oscillation when data are filtered to retain only the  
626 20-100 day variability. Figure 11b and 11c show the same plot, but from our two models in CMIP5 and  
627 CMIP6. Although the new model is far from realistic in terms of eastward propagation, there is indeed a  
628 clear improvement compared to the old one.

629 MJO can also exert impacts on weather and climate of extra-tropics, either through emanation of  
630 Rossby waves, or the poleward propagation of MJO itself. Figure 11d shows a latitude-time diagram for  
631 lagged correlation coefficients when rainfalls are filtered to only retain the variability of 20-100 days.  
632 Panels e and f in Figure 11 are the counterpart simulated by our two models. The new model presents a  
633 clear improvement.

#### 634 **4.5 Interannual variation of sea surface temperature (SST) in the equatorial Pacific**

635 Figure 12 shows the observed and simulated spatial pattern of standard deviation of SST anomalies  
636 in the tropical Pacific. Both BCC-CSM2-MR and BCC-CSM1.1m can simulate the position of the  
637 strongest variation of SST, situated in the central-eastern Pacific in the east of the dateline. However,  
638 cold SST in the eastern equatorial Pacific still extends too far west in both models and a cold tongue  
639 bias exists in the equatorial Pacific and even gets a little worse in BCC-CSM2-MR. The annual mean  
640 SST in the coldest center near  $110^{\circ}\text{W}$  in the equatorial Pacific is below  $23^{\circ}\text{C}$  in BCC-CSM2-MR, a  
641 deterioration compared to BCC-CSM1.1m. As shown in Figure 12a, HadISST observations (Rayner et  
642 al., 2003) can clearly identify a zone of large interannual variation of SST from the Peruvian coast to  
643 the equatorial cold tongue. It is well simulated in BCC-CSM2-MR, but almost missing in  
644 BCC-CSM1.1m.

645 Figure 13 presents time series of the monthly Nino3.4 SST Index from observations and from  
646 simulations of BCC-CSM1.1m and BCC-CSM2-MR. Although amplitudes of interannual variations of  
647 the Nino3.4 index in both models are larger than in HadISST observations, it gets weaker in  
648 BCC-CSM2-MR with standard deviation of  $0.91^{\circ}\text{C}$  which is close to observation showing standard  
649 deviation of  $0.79^{\circ}\text{C}$ . Recent studies of Lu and Ren (2016) reveal that the mean period ENSO in  
650 BCC-CSM1.1m is only 2.4 years, much shorter than that in observation. This bias of a too-short



651 periodicity of the ENSO cycle still persists in BCC-CSM2-MR. Nevertheless, The characteristic of  
652 ENSO irregularity is improved in BCC-CSM2-MR in comparison to BCC-CSM1.1m.

#### 653 **4.6 Sea ice state and oceanic overturning circulation**

654 Figure 14 shows time-series of minimum sea-ice extent from 1851 to 2012 for (a) the Arctic in  
655 September and (b) the Antarctic in March as simulated in BCC-CSM2-MR and BCC-CSM1.1m. Base  
656 on Hadley Centre Sea Ice and Sea Surface Temperature data set (Rayner et al., 2003, shown by “Hadley”  
657 in Figure 14), the observed minimum sea-ice extent in each September from 1851 to 2012 gradually  
658 shrinks, especially since the 1960’s, as caused by global warming (Figure 4). The extent of Arctic sea  
659 ice in September in BCC-CSM1.1m is about  $2 \times 10^6$  km<sup>2</sup> smaller than the Hadley Centre data, and it  
660 begins to shrink since the 1910’s, earlier than in observations. Although the Arctic sea-ice extent in  
661 September in BCC-CSM2-MR is even further smaller than in BCC-CSM1.1m, the model performance  
662 is improved since the 1960’s and becomes closer to the Hadley observation. In Figure 14b, it is to be  
663 noted that the Antarctic minimum sea-ice extent in the new model is very small, almost a half of what  
664 observed. The old model had however a more realistic behavior for this regard. This discrepancy is  
665 related to too-warm temperatures simulated in BCC-CSM2-MR in the Southern Ocean, in particular in  
666 the Weddell Sea. The downward trend in the Arctic summer sea-ice extent is, however, better simulated  
667 in the new model than in the old one.

668 Figure 15 shows the seasonal cycle of sea ice extent (SIE) and thickness averaged for the period of  
669 1980 to 2005 in the two Polar Regions in our models. Observations of sea ice extent from the Hadley  
670 Centre data and sea ice thickness from the European Centre for Medium-Range Weather Forecasts  
671 (ECMWF) are also plotted for the purpose of comparison. Observations show that the Arctic sea ice  
672 cover reaches a minimum extent of  $6.9 \times 10^6$  km<sup>2</sup> in September and rises to a maximum extent of  
673  $16.0 \times 10^6$  km<sup>2</sup> in March (Fig. 15a). The two models can both capture the seasonal variation and pattern,  
674 but large biases in BCC-CSM1.1m exist in magnitude, especially in boreal winter, which is evidently  
675 improved in BCC-CSM2-MR. As for Antarctic SIE (Fig. 15b), the ice covers in two models also  
676 undergo a very large seasonal cycle, which is similar to observations. However, SIE in BCC-CSM1.1m  
677 is too extensive nearly throughout the year, particularly in southern hemisphere winter. Comparatively,  
678 the new model BCC-CSM2-MR simulates a relatively smaller seasonal cycle than that in BCC-CSM1.1

679 and closer to observations except in February to March. In terms of ice thickness (Fig. 15c and d), the  
680 two models simulate a thinner ice cover compared to observations in all seasons for both the Arctic and  
681 Antarctic. The most remarkable improvements of BCC-CSM2-MR appear in the Arctic in the boreal  
682 warm seasons, especially from June to September with thicker ice presented in the Arctic Ocean. Those  
683 improvements may be partly achieved with the new model physics such as schemes for turbulent flux  
684 over sea ice and ocean surfaces, cloud fraction, or atmospheric circulation improvements at high  
685 latitudes. But in the Antarctic, the ice thickness in BCC-CSM2-MR gets worse and even much thinner  
686 than that in BCC-CSM1.1m in almost all the year.

687 The Atlantic Meridional Overturning Circulation (AMOC) plays a significant role in driving the  
688 global climate variation (Caesar et al., 2018). AMOC consists of two primary overturning cells. In the  
689 upper cell, warm water flows northward in the upper 1000 m to supply the formation of the North  
690 Atlantic Deep Water (NADW), which returns southward in the depth range of approximately 1500 to  
691 4000 m. In contrast, in the lower cell, the Antarctic Bottom Water (AABW) flows northward in the  
692 Atlantic basin beneath NADW. Figure 16 shows the time-averaged AMOC simulated by the two  
693 coupled model versions. The two main cells are well depicted. The lower branch of NADW is much  
694 deeper in BCC-CSM2-MR than in BCC-CSM1.1m, as indicated by the depth of the zero-contour line.  
695 Moreover, the central intensity of NADW in BCC-CSM2-MR is over 22.5 Sv about 2.5 Sv stronger  
696 than that in BCC-CSM1.1m, close to observation-based value (25 Sv in Talley et al., 2013).

#### 697 **4.7 Evaluation of models for their performance in East Asia**

698 A good simulation of climate over East Asia is always a challenging issue for the climate modelling  
699 community, as the region is under influences of complex topography (high Tibetan Plateau), and  
700 atmospheric circulations from low latitudes (tropical monsoon circulation) and from higher latitudes.  
701 Figure 17 plots a Taylor diagram to show models performance of main climate variables over East Asia  
702 covering the region (100 °-140 °E, 20 °-50 °N). Both BCC-CSM1.1m (blue figures) and BCC-CSM2-MR  
703 (red figures) are plotted for precipitation, sea-level pressure and variables of the atmospheric general  
704 circulation. There is a clear and remarkable improvement from CMIP5 to CMIP6 in BCC models. The  
705 amelioration is both in the spatial pattern correlation (radial lines) and in the ratio of standard deviations  
706 (circles from the origin).

707 Figure 18 shows the 1980-2005 climatology of December-January-February and June-July-August  
708 averaged precipitation over China and its surroundings. In boreal winter, GPCP precipitations show a  
709 rain belt from Southeast China to Japan and another rain belt along the southwestern flank of the  
710 Tibetan Plateau. In BCC-CSM1.1m the winter precipitation is too weak in Southeast China and too  
711 strong near Japan, compared to GPCP observations. This rain belt in BCC-CSM2-MR obviously  
712 spreads westward and is much closer to observations. The rain belt along the southwestern flank of the  
713 Tibetan Plateau in BCC-CSM2-MR, however, gets too strong. In boreal summer, large dry biases over  
714 East China are present in BCC-CSM1.1m. Those biases are reduced in BCC-CSM2-MR. The center of  
715 precipitation around Japan is also well simulated in BCC-CSM2-MR.

716 The East Asian summer monsoon rainfall has a seasonal progression from south to north at the  
717 beginning of summer and then a quick retreat to the south when the summer monsoon terminates (as  
718 shown in Figure 19a). This phenomenon is strongly related to the fact that the East Asian monsoon  
719 rainfall mainly takes place in the frontal zone between warm and humid air mass from the south, and  
720 cold and dry air mass from the north. This seasonal migration is also accompanied with a meridional  
721 movement of the Western North Pacific Subtropical High, an important atmospheric center of action  
722 controlling the climate of the region. In Figure 19 (panels b and c), we compare the two models in terms  
723 of seasonal migration of the monsoon rainfall. In the old model, rainfall was too weak. The new model  
724 produces more precipitation. In terms of seasonal match, both models show a delay of the peak rainfall  
725 by about one month, even longer in BCC-CSM2-MR.

726 Finally, let us examine the rainfall diurnal cycle in summer. Figure 20 shows the timing of the  
727 rainfall diurnal cycle from observation and the two models. Main zones of nocturne rainfall can be  
728 recognized in the south flank of the Tibetan Plateau, in the Sichuan Basin in the east of the Tibetan  
729 Plateau, and in the north of Xinjiang in Central Asia. There is also a zone of nocturne rainfall in the low  
730 reach of the Yellow River. This is mainly under the influence of nocturne rainfall in the area of the  
731 Bohai Sea. Other regions over land experience diurnal rainfall peak in the afternoon after 16 hours local  
732 time. The diurnal cycle of rainfall was extensively studied in Jin et al. (2013) in terms of physics  
733 causing the diurnal cycle. But the good simulation of diurnal cycle is always a major challenge for  
734 climate modeling. We can see that it is not very well simulated in our old model and in East China the

735 peak occurs in the mid and later night (0-4 am). But the improvement is quite spectacular in our new  
736 model with rainfall peak delayed in the afternoon. Such an improvement is due to the implementation of  
737 our new trigger scheme in convection parameterization.

## 738 **5. Conclusions and discussion**

739 This paper presents the main progress of BCC climate system models from CMIP5 to CMIP6 and  
740 focuses on the description of CMIP6 version BCC-CSM2-MR and CMIP5 version BCC-CSM1.1m  
741 especially on the model physics. Main updates in model physics include a modification of deep  
742 convection parameterization, a new scheme for cloud fraction, indirect effects of aerosols through  
743 clouds and precipitation, and the gravity wave drag generated by deep convection. Surface processes in  
744 BCC-AVIM have also been significantly improved for soil water freezing treatment, snow aging effect  
745 on surface albedo, and timing of vegetation leaf unfolding, growth, and withering. A four-stream  
746 radiation transfer within the vegetation canopy replaced the two-stream radiation transfer. There is a  
747 new treatment for rice paddy waters. New schemes for surface turbulent fluxes of momentum, heat and  
748 water at the interface of atmosphere and sea/sea ice are also used.

749 The evaluation of model performance in simulating present-day climatology is presented for main  
750 climate variables, such as, surface air temperature, precipitation, and atmospheric circulation for the  
751 globe and for East Asia. Emphasis is put on comparison between the CMIP5 and CMIP6 model  
752 versions (BCC-CSM2-MR versus BCC-CSM1.1m). The globally-averaged TOA net energy budget is  
753  $0.85 \text{ W} \cdot \text{m}^{-2}$  in BCC-CSM2-MR, and  $0.98 \text{ W} \cdot \text{m}^{-2}$  in BCC-CSM1.1m. Both versions have a very good  
754 energy equilibrium. Model biases of excessive cloud shortwave and longwave radiative forcings over  
755 low latitudes in BCC-CSM1.1m are obviously reduced in BCC-CSM2-MR. When Taylor diagrams are  
756 used to compare the two models for spatial patterns of main climate variables such as 2-meter surface  
757 air temperature, precipitation, and atmospheric general circulation, BCC-CSM2-MR shows an overall  
758 improvement at both global scale and regional scale in East Asia. These improvements in  
759 BCC-CSM2-MR are believed to be achieved by the new scheme of cloud fraction and by the  
760 consideration of indirect effects of aerosol on clouds and precipitation. The cold tongue bias of SST in  
761 the equatorial Pacific in BCC-CSM1.1m still exists in BCC-CSM2-MR. BCC-CSM1.1m has a severe  
762 bias in sea ice extent (SIE) and thickness (Tan et al., 2015): too extensive in cold seasons and less

763 extensive in warm seasons in both hemispheres. The most impressive improvements in  
764 BCC-CSM2-MR appear in the boreal warm seasons, especially from June to September with thicker ice  
765 presented in the Arctic Ocean. However, in the Southern Hemisphere, the sea ice extent and thickness in  
766 BCC-CSM2-MR become even smaller than those in its previous version. This is still an issue that needs  
767 to be addressed in our future work. There is another model bias of weak oceanic overturning circulation  
768 in BCC-CSM1.1m. This bias is reduced in the new version BCC-CSM2-MR, and the strength of  
769 AMOC is increased.

770 Further evaluations are performed on climate variabilities at different time scales, including  
771 long-term trend of global warming in the 20<sup>th</sup> century, QBO, MJO, and diurnal cycle of precipitation.  
772 The globally-averaged annual-mean surface air temperature from the historical simulation of  
773 BCC-CSM2-MR is much closer to HadCRUT4 observation than BCC-CSM1.1m, and the observed  
774 global warming hiatus or warming slowdown in the period from 1998 to 2013 is captured in some  
775 realization of BCC-CSM2-MR. With a higher vertical resolution and inclusion of the gravity wave drag  
776 generated by deep convection, the new version BCC-CSM2-MR is able to reproduce the stratospheric  
777 QBO, while QBO even does not exist in BCC-CSM1.1m. Further investigations on physical  
778 mechanisms controlling QBO simulation in BCC-CSM2-MR will be reported in future. MJO is a very  
779 important atmospheric oscillation at intra-seasonal scales and main features are reproduced and  
780 improved in BCC-CSM2-MR, but with intensity still weaker than its counterpart in observation. At  
781 interannual scale, BCC-CSM1.1m shows too-strong variations of Nino 3.4 SST index, but too-short and  
782 too-regular periodicity for ENSO. BCC-CSM2-MR shows weaker amplitude for Nino 3.4 SST index,  
783 which is an improvement and closer to HadISST observations. The rainfall diurnal cycle in China has  
784 strong regional variations with pronounced nocturne rainfalls in the Sichuan Basin and in north China  
785 near the Bohai Sea and the coast. The diurnal rainfall generally peaks in the local time afternoon for  
786 most other land regions. BCC-CSM2-MR shows a clear improvement of rainfall diurnal peaks  
787 compared to the CMIP5 model (BCC-CSM1.1m). This improvement of rainfall diurnal variation is  
788 strongly related to the modification of deep convection scheme.

789 Finally, we also evaluate the climate sensitivity to CO<sub>2</sub> increasing in the standard simulation of 1%  
790 CO<sub>2</sub> increase per year (1pctCO<sub>2</sub>) and the 4xCO<sub>2</sub> abrupt-change. The transient climate response in the

791 new CMIP6 model version BCC-CSM2-MR is lower than that in the previous CMIP5 model  
792 BCC-CSM1.1m, while the equilibrium climate sensitivity ECS for BCC-CSM2-MR is slightly higher  
793 than its counterpart in BCC-CSM1.1m.

794 From our model evaluations, we find that although basic feature of the QBO can be simulated in  
795 BCC-CSM2-MR, the magnitude between westerly and easterly interchange is still too weak. We also  
796 note that there are large biases of air temperature and winds in the stratosphere. Therefore, improvement  
797 of the stratospheric temperature and circulation simulations is an important priority in the future  
798 development of BCC models. In addition, sea ice simulation in the Antarctic region has large biases,  
799 which need to be improved.

## 800 **6. Code and data availability**

801 Source codes of BCC models are freely available upon request addressed to Tongwen Wu  
802 (twwu@cma.gov.cn). Model output of BCC models for both CMIP5 and CMIP6 simulations described  
803 in this paper is distributed through the Earth System Grid Federation (ESGF) and freely accessible  
804 through the ESGF data portals after registration. Details about ESGF are presented on the CMIP Panel  
805 website at <http://www.wcrp-climate.org/index.php/wgcm-cmip/about-cmip>.

806

## 807 **Author contributions**

808 Tongwen Wu led the BCC-CSM development. Tongwen Wu and Xiaoge Xin designed the experiments  
809 and carried them out. Tongwen Wu, Laurent Li, and Xiaohong Liu wrote the final document with  
810 contributions from all other authors.

811

## 812 **Acknowledgements**

813 This work was supported by The National Key Research and Development Program of China  
814 (2016YFA0602100). Two anonymous reviewers are acknowledged for their constructive comments on  
815 earlier versions of the paper.

## 816 **References**

817 Albrecht, B.: Aerosols, cloud microphysics, and fractional cloudiness, *Science*, 245, 1227–1230, 1989.  
818 Adler, R. F., Chang, A.: The Version 2 Global Precipitation Climatology Project (GPCP) Monthly Precipitation

819 Analysis (1979-Present), *J. Hydrometeor.*, 4, 1147–1167, 2003

820 Alexander, M. J., May, P. T., and Beres, J. H.: Gravity waves generated by convection in the Darwin area during  
821 the Darwin Area Wave Experiment, *J. Geophys. Res.*, 109, D20S04, doi: 10.1029/2004JD004729, 2004.

822 Allen, M., Stott, P., Mitchell, J., Schnur, R., and Delworth, T.: Quantifying the uncertainty in forecasts of  
823 anthropogenic climate change, *Nature*, 407, 617-620, 2000.

824 Arora, V. K., and Boer, G. J.: A parameterization of leaf phenology for the terrestrial ecosystem component of  
825 climate models, *Global Change Biology*, 11, 39-59, doi:10.1111/j.1365-2486.2004.00890.x, 2005.

826 Andreas, E. L.: A theory for the scalar roughness and the scalar transfer coefficients over snow and sea ice,  
827 *Bound.-Layer Meteor.*, 38, 159-184, 1987.

828 Andreas, E. L.: Parameterizing scalar transfer over snow and ice: A review, *Journal of Hydrometeorology*, 3,  
829 417-432, 2002.

830 Andreas, E. L., Horst, T. W., Grachev, A. A., Persson, P. O. G., Fairall, C. W., and Guest, P. S., and Jordan, R.E.:  
831 Parametrizing turbulent exchange over summer sea ice and the marginal ice zone, *Quarterly Journal of the*  
832 *Royal Meteorological Society*, 136, 927-943, 2010a.

833 Andreas, E. L., Persson, P. G., Jordan, R. E., Horst, T.W., Guest, T.S., Grachev, A.A., and Fairall, C.W.:  
834 Parameterizing turbulent exchange over sea ice in winter, *Journal of Hydrometeorology*, 11, 87-104, 2010b.

835 Andrews, T., Gregory, J. M., Webb, M. J., and, K. E.: Forcing, feedbacks and climate sensitivity in CMIP5  
836 coupled atmosphereocean climate models, *Geophys. Res. Lett.*, 38, L09712, doi: 10.1029/2012GL051607,  
837 2012.

838 Beres, J. H., Alexander, M. J., and Holton, J. R.: A method of specifying the gravity wave spectrum above  
839 convection based on latent heating properties and background wind, *J. Atmos. Sci.*, 61, 324-337, 2004.

840 Boucher, O., Lohmann, U.: The sulphate-CCN-cloud albedo effect – a sensitivity study with two general  
841 circulation models, *Tellus* 47B, 281–300, 1995.

842 Caesar, L., Rahmstorf, S., Robinson, A., Feulner, G., Saba, V.: Observed fingerprint of a weakening Atlantic  
843 Ocean overturning circulation, *Nature*, 556, 191-196, 2018.

844 Campin J.M., and Goosse, H.: Parameterization of density-driven downsloping flow for a coarse-resolution ocean  
845 model in z-coordinate, *Tellus*, 51A, 412–430, 1999.

846 Cao M., and Woodward F. I.: Net primary and ecosystem production and carbon stocks of terrestrial ecosystems  
847 and their responses to climate change, *Global Change Biology*, 4, 185-198, 1998.

848 Chen C., and Cotton, W. R.: The physics of the marine stratocumulus-capped mixed layer, *J. Atmos. Sci.*, 44 (50),

849 2951–2977, 1987.

850 Chen A., Li, W. P., Li, W. J., and Liu, X.: An observational study of snow aging and the seasonal variation of  
851 snow albedo by using data from Col de Porte, France. *Chinese Science Bulletin*, 59 (34), 4881-4889, 2014

852 Collins, W. D., Rasch, P.J., Boville, B.A., Hack, J. J., McCaa, J.R., Williamson, D. L., Kiehl, J. T., Briegleb, B.,  
853 Bitz C., Lin S.J., Zhang, M.H., and Dai, Y.J.: Description of the NCAR community atmosphere model  
854 (CAM3). Technical Report NCAR/TN-464 + STR, National Center for Atmospheric Research, Boulder,  
855 Colorado, 226 pp, 2004.

856 Collins, W. J., Lamarque, J.–F., Schulz, M., Boucher, O., Eyring, V., Hegglin, M. I., Maycock, A., Myhre, G.,  
857 Prather, M., Shindell, D., and Smith, S. J.: AerChemMIP: quantifying the effects of chemistry and aerosols  
858 in CMIP6, *Geosci. Model Dev.*, 10, 585–607, 2017.

859 Danabasoglu, G., and Co-authors: North Atlantic simulations in Coordinated Ocean-ice Reference  
860 Experiments phase II (CORE-II). Part I: Mean States. *Ocean Modelling*, 73, 76-107, doi:  
861 10.1016/j.ocemod.2013.10.005, 2014.

862 Dee, D.P., Uppala, S. M., Simmons, A. J., Berrisford, P., Poli, P., Kobayashi, S., Andrae, U., Balmaseda, M. A.,  
863 Balsamo, G., Bauer, P., Bechtold, P., Beljaars, A. C. M., Berg L., Bidlot, J., Bormann, N., Delsol, C., Dragani,  
864 R., Fuentes, M., Geer, A. J., Haimberger, L., Healy, S. B., Hersbach, H., Holm, E. V., Isaksen, L., Kallberg, P.,  
865 Kohler, M., Matricardi, M., McNally, A.P., Monge-Sanz, B. M., Morcrette, J.-J., Park, B.-K., Peubey, C.,  
866 Rosnay, P., Tavolato, C., Thepaut, J.-N., and Vitart F.: The ERA-Interim reanalysis: configuration and  
867 performance of the data assimilation system, *Quart. J. R. Meteorol. Soc.*, 137, 553-597 (DOI:  
868 10.1002/qj.828) , 2011.

869 Ding, Y. H., Liu, Y. M., Song, Y. J., Li, Q. Q.: Research and experiments of the dynamical model system for  
870 short-term climate prediction, *Climatic Environ. Res.*, 7(2), 236–246, 2002 (in Chinese).

871 Eyring, V., Bony, S., Meehl, G. A., Senior, C. A., Stevens, B., Stouffer, R. J., Taylor, K. E.: Overview of the  
872 Coupled Model Intercomparison Project Phase 6 (CMIP6) experimental design and organization, *Geosci.*  
873 *Model Dev.*, 9, 1937–1958, 2016, 2017.

874 Fetterer, F., Knowles, K., Meier, W., Savoie, M.: Sea Ice Index, digital media, National Snow and Ice Data Center.  
875 Boulder, CO., 2002.

876 Fyfe, J.C., Meehl, G.A., England, M.H., Mann, M. E. Santer, B. D., Flato, G. M., Hawkins, E., Gillett, N. P., Xie,  
877 S.–P., Kosaka, Y., Swart, N. C.: Making sense of the early-2000s warming slowdown, *Nat. Clim. Change* 6,  
878 224–228, 2016.



879 Griffies, S. M., Gnanadesikan, A., Dixon, K. W., Dunne, J. P., Gerdes, R., Harrison, M. J., Rosati, A., Lin, J.,  
880 Bonita, R., Samuels, L., Spelman, M. J., Winton, M., Zhang, R.J.: Formulation of an ocean model for  
881 global climate simulations, *Ocean Sci.*, 1, 45–79, 2005.

882 Gregory, J. M., Ingram, W. J., Palmer, M. A., Jones, G. S., Stott, P. A., Thorpe, R. B., Lowe, J. A., Johns, T. C.,  
883 and Williams, K. D.: A new method for diagnosing radiative forcing and climate sensitivity, *Geophys. Res.*  
884 *Let.*, 31, L03205, doi:10.1029/2003GL018747, 2004.

885 Gregory, J.M., Webb, M. J., and Taylor, K. E.: Forcing, feedbacks and climate sensitivity in CMIP5 coupled  
886 atmosphere-ocean climate models, *Geophys. Res. Let.*, 39, L09712, doi:10.1029/2012GL051607, 2012.

887 Gent, P. R., McWilliams, J. C.: Isopycnal mixing in ocean circulation Models[J]. *Journal of Physical*  
888 *Oceanography*, 20(1), 150–155, 1990.

889 Guenther, A. B., Jiang, X., Heald, C. L., Sakulyanontvittaya, T., Duhl, T., Emmons, L. K., and Wang, X.: The  
890 Model of Emissions of Gases and Aerosols from Nature Version 2.1 (MEGAN2.1): An Extended and  
891 Updated Framework for Modeling Biogenic Emissions, *Geoscientific Model Development* 5(6): 1471–1492,  
892 2012.

893 Hack, J. J., Parameterization of moist convection in the National Center for Atmospheric Research Community  
894 Climate Model (CCM2), *J. Geophys. Res.*, 99, 5551–5568, 1994.

895 Haarsma, R. J., Roberts, M. J., Vidale, P. L., Senior, C. A., Bellucci, A., Bao, Q., Chang, P., Corti, S., Fuckar, N.  
896 S., Guemas, V., Hardenberg, J. von, Hazeleger, W., Kodama, C., Koenigk, T., Leung, L. R., Lu, J., Luo, J. –J.,  
897 Mao, J., Mizielinski, M. S., Mizuta, R. Nobre, P., Satoh, M., Scoccimarro, E., Semmler, T., Small, J., and  
898 Storch, J.–S. von : High Resolution Model Intercomparison Project (HighResMIP v1.0) for CMIP6, *Geosci.*  
899 *Model Dev.*, 9, 4185–4208, doi:10.5194/gmd-9-4185-2016, 2016.

900 Holtlag, A. A. M., and Boville, B. A.: Local versus nonlocal boundary-layer diffusion in a global climate model,  
901 *J. Climate*, 6, 1825–1842, 1993.

902 Huffman, G., Bolvin, D., Braithwaite, D., Hsu, K., Joyce, R., Xie, P.: Integrated Multi-satellite Retrievals for  
903 GPM (IMERG), version 4.4. NASA's Precipitation Processing Center, accessed 31 March, 2015,  
904 ftp://arthurhou.pps.eosdis.nasa.gov/gpmdata/, 2014.

905 IPCC Climate Change: The Physical Science Basis (eds Stocker, T. F., Qin, D., Plattner, G.-K., Tignor, M., Allen,  
906 S. K., Boschung, J., Nauels, A., Xia, Y., Bex V., and Midgley, P. M.) , Cambridge Univ. Press, Cambridge,  
907 United Kingdom and New York, NY, USA, 2013.

908 Ji, J.: A climate-vegetation interaction model: Simulating physical and biological processes at the surface, *Journal*

909 of Biogeography, 22, 2063-2069, 1995.

910 Ji, J., Huang, M., and Li, K.: Prediction of carbon exchange between China terrestrial ecosystem and atmosphere  
911 in 21st century, *Sci. China Ser. D: Earth Sci.*, 51(6), 885-898, 2008.

912 Li, J. D., Wang, W.-C., Liao, H., and Chang, W. Y.: Past and future direct radiative forcing of nitrate aerosol in  
913 East Asia, *Theoretical and Applied Climatology*, 121, 445-458, 2015.

914 Lu, B., Ren, H.-L.: Improving ENSO periodicity simulation by adjusting cumulus entrainment in BCC\_CSMs,  
915 *Dynamics of Atmospheres and Oceans*, 76, 127-140, 2016.

916 Jiang X., Waliser, D. E., Xavier, P.K., Petch, J., Klingaman, N. P., Woolnough, S.J., Guan, B., Bellon, G., Crueger,  
917 T., DeMott, C., Hannay, C., Lin, H., Hu, W., Kim, D., Lappen, C., Lu, M.-M., Ma, H.-Y., Miyakawa, T.,  
918 Ridout, J. A., Schubert, S.D., Scinocca, J., Seo, K.-H., Shindo, E., Song, X., Stan, C., Tseng, W.-L., Wang,  
919 W., Wu, T., Wyser, K., Wu, X., Zhang, G. J., Zhu, H.: Exploring Key Processes of the Madden-Julian  
920 Oscillation (MJO): A Joint WGENE MJO Task Force / GEWEX GASS Project on the Vertical Structure and  
921 Diabatic Processes of the MJO – Part I. Climate Simulations, *J. Geophys. Res. Atmos.*, 120, 4718–4748.  
922 doi:10.1002/2014JD022375, 2015.

923 Jin, X., Wu, T., Li, L.: The quasi-stationary feature of nocturnal precipitation in the Sichuan Basin and the role of  
924 the Tibetan Plateau, *Climate Dynamics*, 41: 977-994. DOI: 10.1007/s00382-012-1521-y, 2013.

925 Jones, C.D., Arora, V., Friedlingstein, P., Bopp, L., Brovkin, V., Dunne, J., Graven, H., Hoffman, F., Ilyina, T.,  
926 John, J. G., Jung, M., Kawamiya, M., Koven, C., Pongratz, J., Raddatz, T., Randerson, J. T., and Zaehle, S.:  
927 C4MIP – The Coupled Climate–Carbon Cycle Model Intercomparison Project: experimental protocol for  
928 CMIP6, *Geosci. Model Dev.*, 9, 2853–2880, doi:10.5194/gmd-9-2853-2016, 2016.

929 Klein, S. A., and Hartmann, D. L.: The seasonal cycle of low stratiform clouds, *J. Climate*, 6, 1587–1606, 1993.

930 Kristjánsson, J. E., Edwards, J. M., Mitchell, D. L.: Impact of a new scheme for optical properties of ice crystals  
931 on climates of two GCMs, *J. Geophys. Res.*, 105(D8), 10063–10079, doi:10.1029/2000JD900015, 2000.

932 Lamarque, J.-F., Emmons, L. K., Hess, P. G., Kinnison, D. E., Tilmes, S., Vitt, F., Heald, C. L., Holland, E. A.,  
933 Lauritzen, P. H., Neu, J., Orlando, J. J., Rasch, P. J., and Tyndall, G. K.: CAM-chem: description and  
934 evaluation of interactive atmospheric chemistry in the Community Earth System Model, *Geosci Model Dev*,  
935 5, 369-411, 2012.

936 Large, W. G., McWilliams, J. C., and Doney, S. C.: Oceanic vertical mixing: A review and a model with a  
937 nonlocal boundary layer parameterization, *Rev. Geophys.*, 32, 363-403, 1994.

938 Liu, Y., and Daum, P. H.: Indirect warming effect from dispersion forcing, *Nature*, 419, 580-581, 2002.

939 Liou, K. N.: An Introduction to Atmospheric Radiation, China Meteorological Press, 313-327 (in Chinese), 2004.

940 Loeb, N.G., Lyman, J.M., Johnson, G.C., Allan, R.P., Doelling, D.R., Wong, T., Soden, B.J., and Stephens, G.L.:  
941 Observed changes in top-of-the-atmosphere radiation and upper-ocean heating consistent within uncertainty,  
942 Nature Geosciences, DOI 10.1038/NGE, 2012.

943 Lu, Y., Zhou, M., and Wu, T.: Validation of parameterizations for the surface turbulent fluxes over sea ice with  
944 CHINARE 2010 and SHEBA data, Polar Research, 32, 20818, <http://dx.doi.org/10.3402/polar.v32i0.20818>,  
945 2013.

946 Meehl, G.A., Boer, G.J., Covey, C., Latif, M., Stouffer, R.J.: Intercomparison makes for a better climate model.  
947 Eos, Trans.Amer.Geophys.Union, 78, 445--451, doi:10.1029/97EO00276.

948 Medhaug, I., Martin, B. S., Erich, M. F., and Knutti, R.: Reconciling controversies about the ‘global warming  
949 hiatus’, Nature, 545, 41–47, 2017.

950 Morice, C. P., Kennedy, J. J., Rayner, N.A., and Jones, P.D.: Quantifying uncertainties in global and regional  
951 temperature change using an ensemble of observational estimates: The HadCRUT4 data set, J. Geophys. Res.  
952 117, D08101, 2012.

953 Martin, G.M., Johnson, D.W., and Spice, A.: The measurement and parameterisation of effective radius of  
954 droplets in warm stratocumulus clouds, J. Atmos. Sci., 51, 1823–1842, 1994.

955 McFarlane, N. A.: The effect of orographically excited gravity wave drag on the general circulation of the lower  
956 stratosphere and troposphere, J. Atmos. Sci., 44, 1775-1800, 1987.

957 Oleson, K. W., Lawrence, D. M. and Dai, Y. J.: Technical description of the Community Land Model (CLM),  
958 NCAR Technical Note NCAR/TN-461+STR, 2004.

959 Pontikis, C.A., and Hicks, E.; Contribution to the cloud droplet effective radius parameterization, Geophys. Res.  
960 Lett. 19, 2227–2230, 1992.

961 Peng, Y., and Lohmann, U.: Sensitivity study of the spectral dispersion of the cloud droplet size distribution on  
962 the indirect aerosol effect, Geophys. Res. Lett., 30(10), 1507, doi:10.1029/2003GL017192, 2003.

963 Quaas J, Boucher O, and Lohmann U: Constraining the total aerosol indirect effect in the LMDZ and ECHAM4  
964 GCMs using MODIS satellite data. Atmos Chem Phys 6,947-955, 2006

965 Rasch, P. J., and Kristj ánsson, J. E.: A comparison of the CCM3 model climate using diagnosed and predicted  
966 condensate parameterizations, J. Climate, 11, 1587-1614, 1998.

967 Rahmstorf, S.: A fast and complete convection scheme for ocean models, Ocean Modelling, 101, 9–11, 1993.

968 Rayner, N. A., Parker, D. E., Horton, E. B., Folland, C., Alexander, L., Rowell, D., Kent, E., and Kaplan, A.:

969 Global analyses of sea surface temperature, sea ice, and night marine air temperature since the late  
970 nineteenth century, *Journal of Geophysical Research*, 108(D14), 4407, doi:10.1029/2002JD002670, 2003.

971 Richter, J. H., Sassi, F., and Garcia, R. R.: Toward a physically based gravity wave source parameterization in a  
972 general circulation model, *J. Atmos. Sci.*, 67, 136--156, 2010.

973 Sweeney, C., Gnanadesikan, A., Griffies, S. M., Harrison, M., Rosati, A., Samuels, B.: Impacts of shortwave  
974 penetration depth on large-scale ocean circulation and heat transport, *Journal of Physical Oceanography* 35,  
975 1103–1119, 2005.

976 Stevens, B., Fiedler, S., Kinne, S., Peters, K., Rast, S., Musse, J., Smith, S.J., and Mauritsen, T.: MACv2-SP: a  
977 parameterization of anthropogenic aerosol optical properties and an associated Twomey effect for use in  
978 CMIP6, *Geos.Mod.Dev.*, 10, 433-452, 2017.

979 Talley, L.D.: Closure of the global overturning circulation through the Indian, Pacific, and Southern Oceans:  
980 Schematics and transports, *Oceanography*, 26, 80–97, 2013.

981 Tan, H.H., Zhang, L.J., Chu, M., Wu, T.W., Qiu, B., and Li, J.L.: An analysis of simulated global sea ice extent,  
982 thickness, and causes of error with the BCC\_CSM model. *Chinese Journal of Atmospheric Sciences* (in  
983 Chinese), 39 (1): 197–209, 2015.

984 Taylor, K. E., Stouffer, R. J., and Meehl, G. A.: An Overview of Cmp5 and the Experiment Design, *B. Am.*  
985 *Meteorol. Soc.*, 93, 485–498, 2012.

986 Tietsche, S., Balmaseda, M., Zuo, H., Mogensen, K.: Arctic sea ice in the ECMWF MyOcean2 ocean reanalysis  
987 ORAP5. Tech Rep 737, European Center for Medium-Range Weather Forecasts, Reading, UK, 2014.

988 Wielicki, B.A., Barkstrom, B. R., Harrison, E. F., Lee, R. B., Smith, G. L., and Cooper, J. E.: Clouds and the  
989 earth's radiant energy system (CERES): an earth observing system experiment, *Bull. Am. Meteorol. Soc.*, 77,  
990 853–868, 1996.

991 Winton, M.: A reformulated three-layer sea ice model, *J. Atmo.Oceanic Technol.*, 17, 525–531, 2000.

992 Wu, T., Song, L., Li, W., Wang, Z., Zhang, H., Xin, X., Zhang, Y., Zhang, L., Li, J., Wu, F., Liu, Y., Zhang, F., Shi,  
993 X., Chu, M., Zhang, J., Fang, Y., Wang, F., Lu, Y., Liu, X., Wei, M., Liu, Q., Zhou, W., Dong, M., Zhao, Q., Ji,  
994 J., Li, L., and Zhou, M.: An overview of BCC climate system model development and application for  
995 climate change studies, *J. Meteor. Res.*, 28(1), 34-56, 2014.

996 Wu, T., Li, W., Ji, J., Xin, X., Li, L., Wang, Z., Zhang, Y., Li, J., Zhang, F., Wei, M., Shi, X., Wu, F., Zhang, L.,  
997 Chu, M., Jie, W., Liu, Y., Wang, F., Liu, X., Li, Q., Dong, M., Liang, X., Gao, Y., and Zhang, J.: Global  
998 carbon budgets simulated by the Beijing climate center climate system model for the last century, *J Geophys*

999 Res Atmos, 118, 4326-4347. doi: 10.1002/jgrd.50320, 2013.

1000 Wu, T.: A Mass-Flux Cumulus Parameterization Scheme for Large-scale Models: Description and Test with  
 1001 Observations, *Clim. Dyn.*, 38:725–744, DOI: 10.1007/s00382-011-0995-3, 2012.

1002 Wu, T., Yu, R., Zhang, F., Wang, Z., Dong, M., Wang, L., Jin, X., Chen, D.L., and Li, L.: The Beijing Climate  
 1003 Center atmospheric general circulation model: description and its performance for the present-day climate,  
 1004 *Climate Dynamics*, 34, 123-147, DOI 10.1007/s00382-008-0487-2, 2010.

1005 Wu, T., Yu, R., and Zhang, F.: A modified dynamic framework for atmospheric spectral model and its application,  
 1006 *J. Atmos.Sci.*, 65, 2235-2253, 2008

1007 Wu, T., and Wu, G.: An empirical formula to compute snow cover fraction in GCMs, *Adv.Atmos.Sci.*, 21,  
 1008 529-535, 2004.

1009 Xia, K., Luo, Y., and Li, W. P.: Simulation of freezing and melting of soil on the northeast Tibetan Plateau.  
 1010 *Chinese Sci. Bull.*, 56, 1-4, doi: 10.1007/s11434-011-4542-8, 2011.

1011 Xin, X., Wu, T., and Zhang, J.: Introduction of CMIP5 experiments carried out with the climate system models of  
 1012 Beijing Climate Center, *Adv. Clim. Change Res.*, 4(1), 41-49, doi: 10.3724/SP.J.1248.2013.041, 2013.

1013 Xu, K. M., and Krueger, S. K.: Evaluation of cloudiness parameterizations using a cumulus ensemble model,  
 1014 *Mon. Wea. Rev.*, 119, 342–367, 1991.

1015 Xu, L., and Penner, J.E.: Global simulations of nitrate and ammonium aerosols and their radiative effects, *Atmos.*  
 1016 *Chem. Phys.*, 12, 9479-9504, 2012.

1017 Zeng, X., Zhao, M., and Dickinson, R. E.: Intercomparison of bulk aerodynamic algorithms for the computation  
 1018 of sea surface fluxes using TOGA COARE and TAO data, *J. Climate*, 11, 2628-2644, 1998.

1019 Zeng, X., Zhang, Q., Johnson, D., and Tao, W.-K.: Parameterization of wind gustiness for the computation of  
 1020 ocean surface fluxes at different spatial scales, *Monthly Weather Review*, 130, 2125-2133, 2002.

1021 Zhang, G.J.: Convective quasi-equilibrium in midlatitude continental environment and its effect on convective  
 1022 parameterization. *J Geophys Res* 107(D14), doi:10.1029/2001JD001005, 2002.

1023 Zhang, M., Lin, W., Bretherton, C. S., Hack, J. J., and Rasch, P. J.: A modified formulation of fractional  
 1024 stratiform condensation rate in the NCAR community atmospheric model CAM2, *J. Geophys. Res.*, 108  
 1025 (D1), 2003.

1026 Zhang, Y., Gao, Z., Li, D., Li, Y., Zhang, N., Zhao, X., and Chen, J.: On the computation of planetary  
 1027 boundary-layer height using the bulk Richardson number method, *Geosci. Model Dev.*, 7, 2599–2611, 2014.

1028 Zhou, W.Y., Luo, Y., Li, W.P., Shi, X.L., and Zhang, Y: Comparative studies of different radiation schemes within

1029      vegetation in land model, Chinese Science Bulletin, 63, 10.1360/N972018-00398, 2018.

Table 1. BCC models for CMIP5 and CMIP6

Model versions	Atmosphere	Atmos Chemistry and Aerosol	Land Surface	Ocean	Sea Ice
BCC-CSM1.1 in CMIP5 (Wu et al., 2013)	BCC-AGCM2.1 (1) T42, 26 layers (2) Top at 2.917 hPa	(1) Prescribed aerosols (2) No atmospheric chemistry (3) Global carbon budget without spatial distribution	BCC-AVIM1.0	MOM4-L40v1 (1) Tri-polar: 0.3 to 1 deg latitude x 1 deg longitude, and 40 layers (2) Oceanic carbon cycle based on OCMIP2	SISv1
BCC-CSM1.1m in CMIP5 (Wu et al., 2013)	BCC-AGCM2.2 (1) T106, 26 layers (2) Top at 2.917 hPa	Same as BCC-CSM1.1	BCC-AVIM1.0	MOM4-L40v2	SISv2
BCC-CSM2-MR In CMIP6	BCC-AGCM3-MR (1) T106, 46 layers (2) Top at 1.459 hPa	(1) Prescribed aerosols (2) No atmospheric chemistry (3) Prognostic spatial CO <sub>2</sub> in the atmosphere	BCC-AVIM2.0	MOM4-L40v2	SISv2
BCC-CSM2-HR In CMIP6	BCC-AGCM3-HR (1) T266, 56 layers (2) Top at 0.092 hPa	(1) Prescribed aerosols (2) No atmospheric chemistry	BCC-AVIM2.0	MOM4-L40v2	SISv2
BCC-ESM1 In CMIP6	BCC-AGCM3-Chem (1) T42, 26 layers (2) Top at 2.917 hPa	(1) Prognostic aerosols (2) MOZART2 atmospheric chemistry	BCC-AVIM2.0	MOM4-L40v2	SISv2

Table 2. Main physics schemes in atmospheric components (BCC-AGCM) of BCC-CSM versions for CMIP5 and CMIP6

	<b>BCC-AGCM2 for CMIP5</b>	<b>BCC-AGCM3 for CMIP6</b>
<b>Deep convection</b>	The cumulus convection parameterization scheme (Wu, 2012)	A modified Wu'2012 scheme described in this work
<b>Shallow/Middle Tropospheric Moist Convection</b>	Hack (1994)	Hack (1994)
<b>Cloud macrophysics</b>	Cloud fraction diagnosed from updraft mass flux and relative humidity (Collins et al., 2004)	A new scheme to diagnose cloud fraction described in this work
<b>Cloud microphysics</b>	Modified scheme of Rasch and Kristj ánsson (1998) by Zhang et al. (2003). No aerosol indirect effects	Modified scheme of Rasch and Kristj ánsson (1998) by Zhang et al. (2003), but included the aerosol indirect effects in which liquid cloud droplet number concentration is diagnosed using the aerosols masses.
<b>gravity wave drag</b>	Gravity wave drag only generated by orography (Mcfarlane 1987)	Gravity wave drag generated by both orography (Mcfarlane 1987) and convection (Beres et al., 2004) using tuned parameters related to model resolutions.
<b>Radiative transfer</b>	Radiative transfer scheme used in CAM3 (Collins et al., 2004) with no aerosol indirect effects, and cloud drop effective radius for clouds is only function of temperature and has a distinct difference between maritime, polar, and continental for warm clouds.	Radiative transfer scheme used in CAM3 (Collins et al., 2004), but including the aerosol indirect effects, and the effective radius of the cloud drop for liquid clouds is diagnosed using liquid cloud droplet number concentration.
<b>Boundary Layer</b>	ABL parameterization [Holtslag and Boville, 1993]	ABL parameterization [Holtslag and Boville, 1993], but modified PBL height computation referred to Zhang et al. (2014)



Table 3. Main physics schemes in BCC-AVIM versions

<b>BCC-AVIM1.0 in CMIP5</b>	<b>BCC-AVIM2.0 in CMIP6</b>
♦ Soil-Vegetation-Atmosphere Transfer module	♦ Modified freeze-thaw scheme for soil water (below 0 degree and dependent on soil & water) (Xia et al., 2011)
♦ Multi-layer snow-soil scheme (same as NCAR CLM3)	♦ Improved parameterization of snow surface albedo (Chen et al., 2014) and snow cover fraction (Wu and Wu, 2004)
♦ Snow Cover Fraction scheme (sub-grid topography)	♦ Four-stream radiation transfer through vegetation canopy (Zhou et al., 2018)
♦ Vegetation growth module	♦ A vegetation phenology similar to Canadian Terrestrial Ecosystem Model (Arora and Boer, 2005)
♦ Soil carbon decomposition module	♦ Parameterized rice paddy scheme
♦ Land use change module (variable crop planting area)	♦ land VOC module (Guenther et al., 2012)

Table 4. Energy balance and cloud radiative forcing at the top-of-atmosphere (TOA) in the model with contrast to CERES/EBAF and CERES observations. Units:  $W \cdot m^{-2}$ .

	BCC-CSM2-MR (CMIP6)	BCC-CSM1.1m (CMIP5)	CERES/EBAF (OBS)	CERES (OBS)
Net energy at TOA	0.85	0.98	0.81	5.73
TOA outgoing longwave radiative flux	239.15	236.10	239.72	238.95
TOA incoming shortwave Radiation	340.46	341.70	340.18	341.47
TOA net shortwave radiative flux	239.09	235.96	240.53	244.68
TOA outgoing longwave radiative flux in clear sky	265.02	265.58	265.80	266.87
TOA net shortwave radiative flux in clear sky	288.67	288.71	287.68	294.69
Shortwave cloud radiative forcing	-49.55	-52.71	-47.16	-48.58
Longwave cloud radiative forcing	25.87	29.48	26.07	27.19

Notes: The model data are the mean of 1986 to 2005, while the available observation data are for 2003–2014.

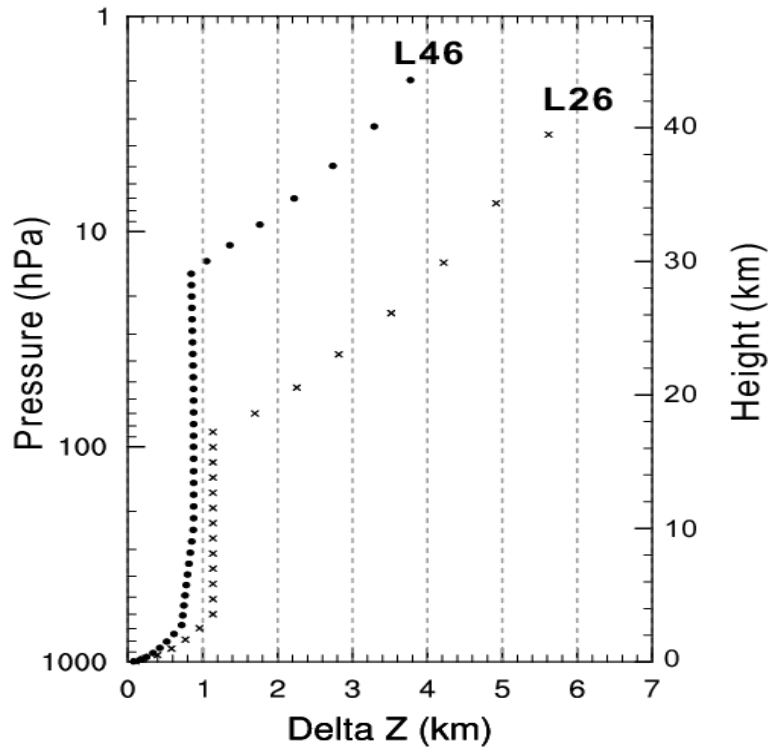


Figure 1. The profiles of layer thickness against the height for 26 vertical layers of the atmosphere in BCC-CSM-1.1m and 46 vertical layers in BCC-CSM2-MR.

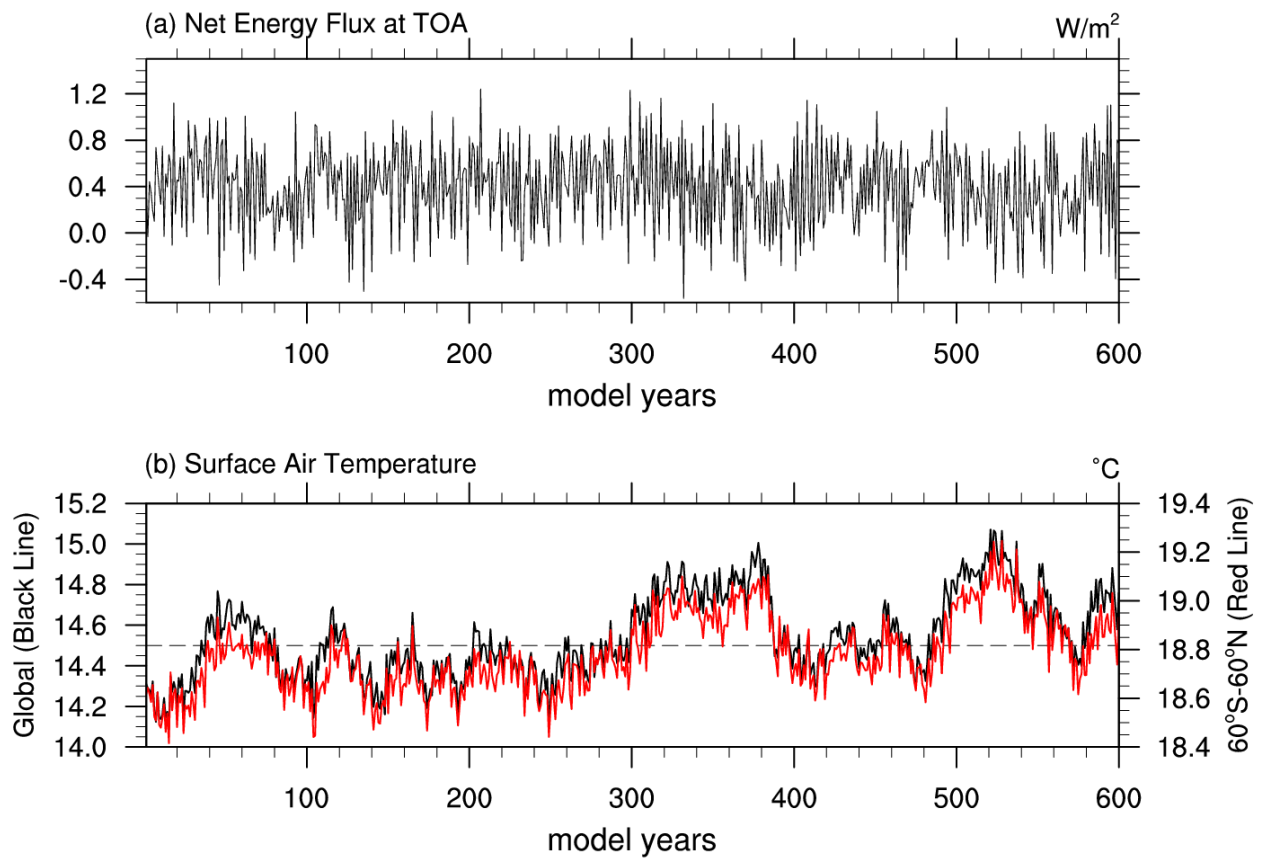


Figure 2. The time series of (a) global mean net energy flux at top of the atmosphere ( $\text{W m}^{-2}$ ) and (b) global (black line) and regional (60°S to 60°N, red line) surface air temperature ( $^{\circ}\text{C}$ ) for the 600 years of piControl simulations.

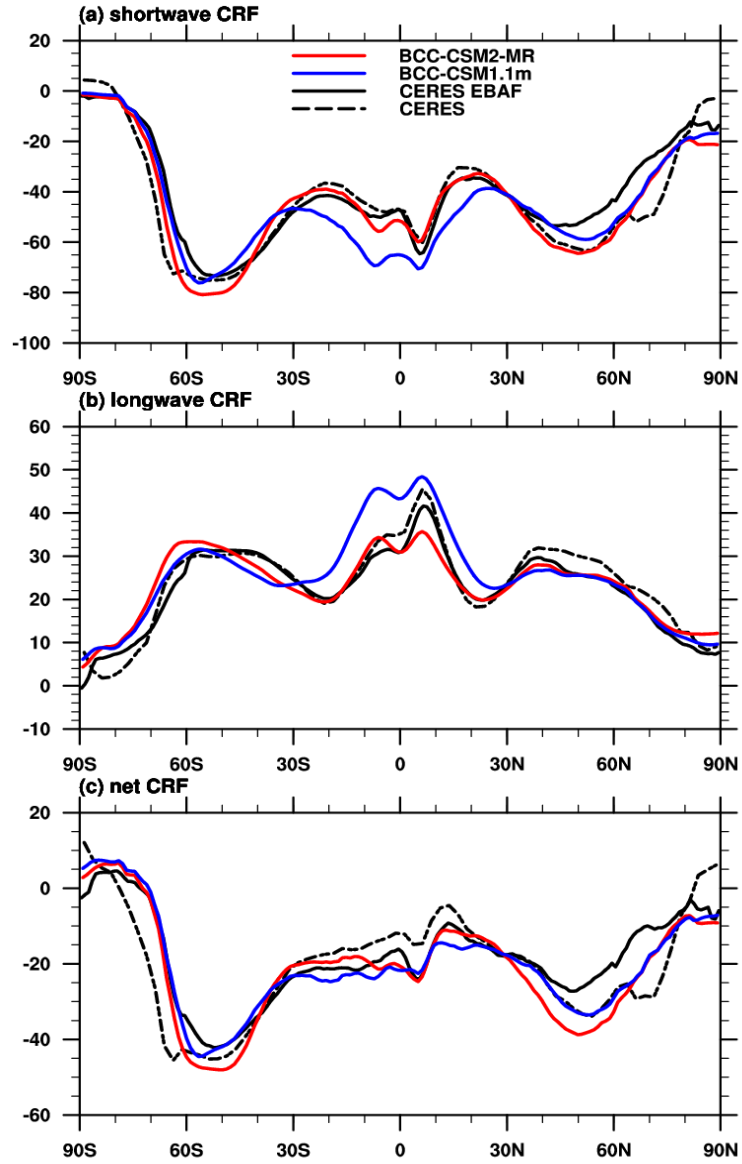


Figure 3. Zonal averages of the cloud radiative forcing from the BCC CMIP5 and CMIP6 models and observations (in  $\text{W m}^{-2}$ ; top row: shortwave effect; middle row: longwave effect; bottom row: net effect). Model results are for the period 1986–2005, while the available CERES ES-4 and CERES EBAF 2.6 data set are for 2003–2014.

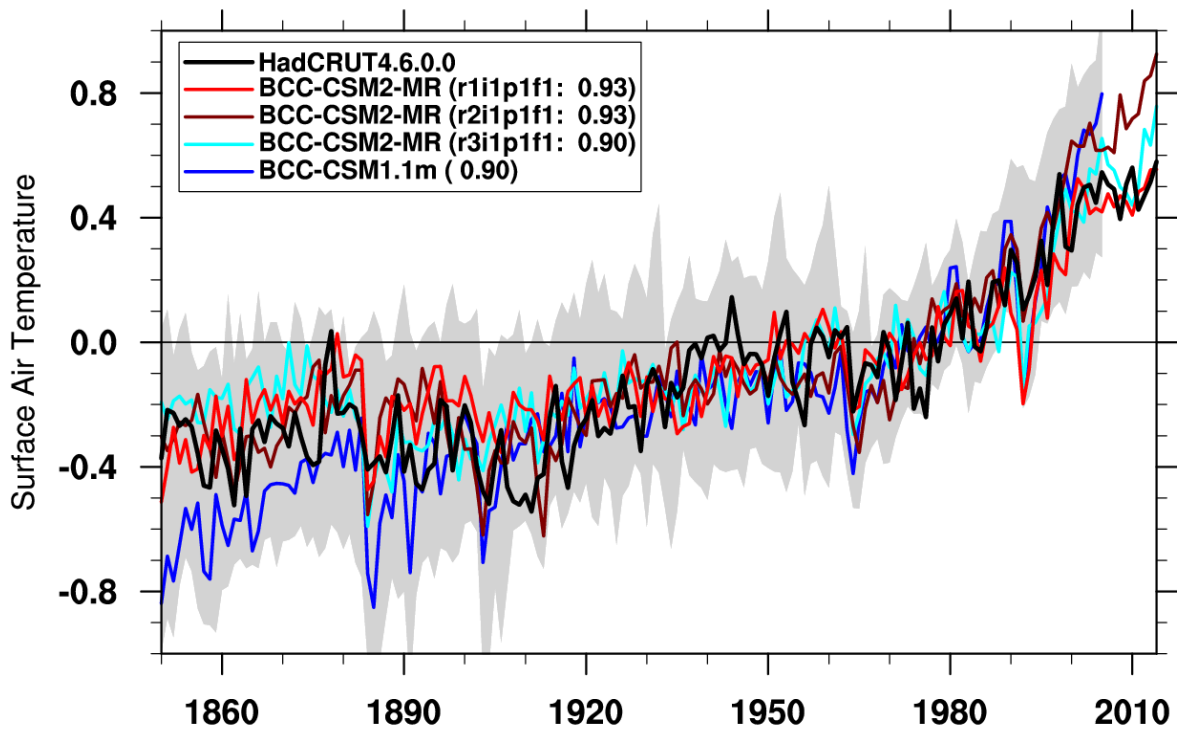


Figure 4. Time series of anomalies in the global (60°S to 60°N) mean surface air temperature from 1850 to 2014. The reference climate to deduce anomalies is for each individual curve from 1961 to 1990. Three lines labeled BCC-CSM2-MR denote three members of historical simulations from different initial state of the piControl simulation. The numbers in the bracket denote the correlation coefficient of 11-year smoothed BCC model data with the HadCRUT4.6.0.0 (Morice et al., 2012) observation. Gray shaded area shows the spread of 36 CMIP5 models data.

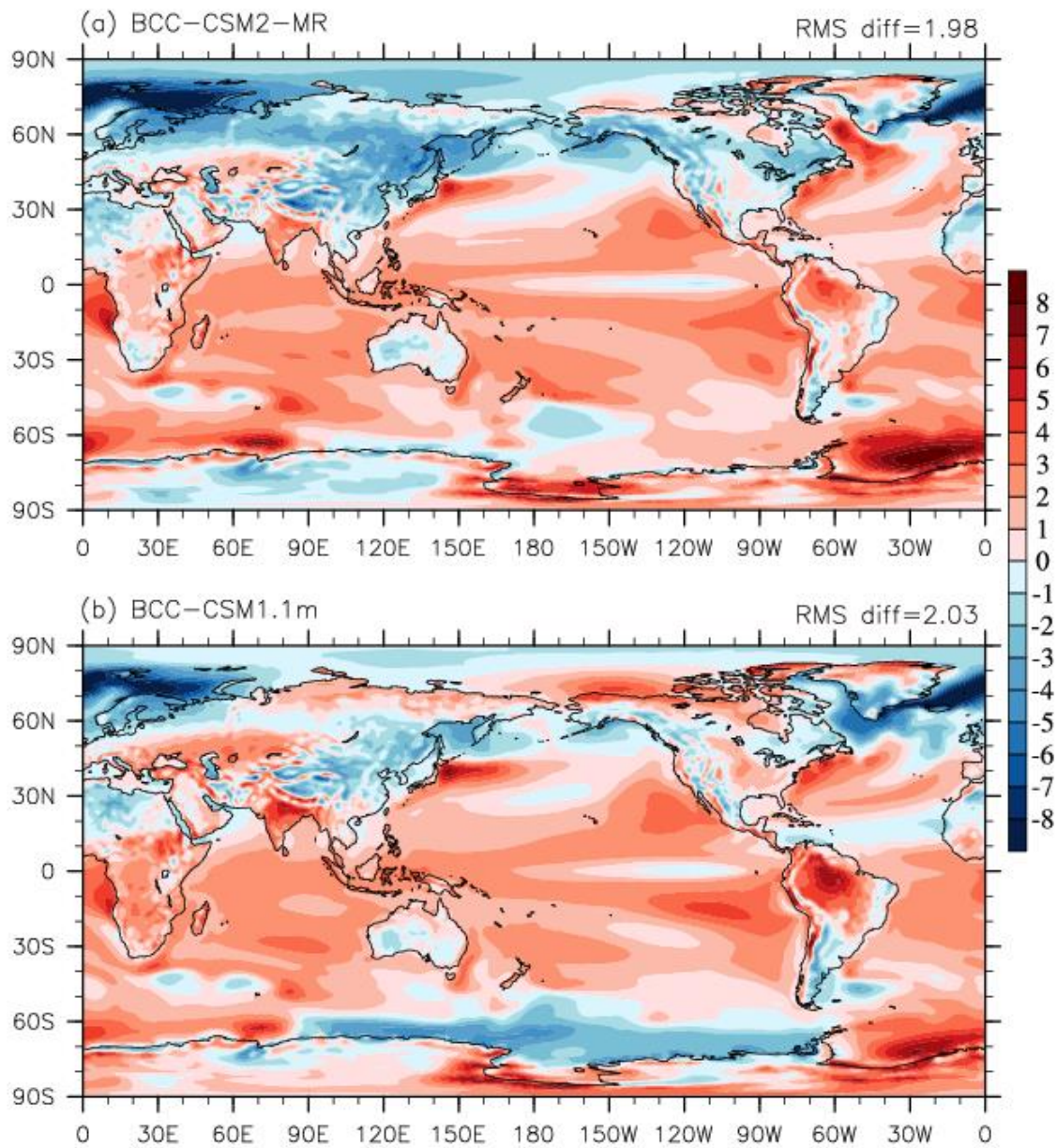


Figure 5. Annual-mean surface (2 meter) air temperature biases ( $^{\circ}\text{C}$ ) of (a) BCC-CSM2-MR and (b) BCC-CSM1.1m simulations with contrast to the reanalysis ERA-Interim for the period of 1986 to 2005.

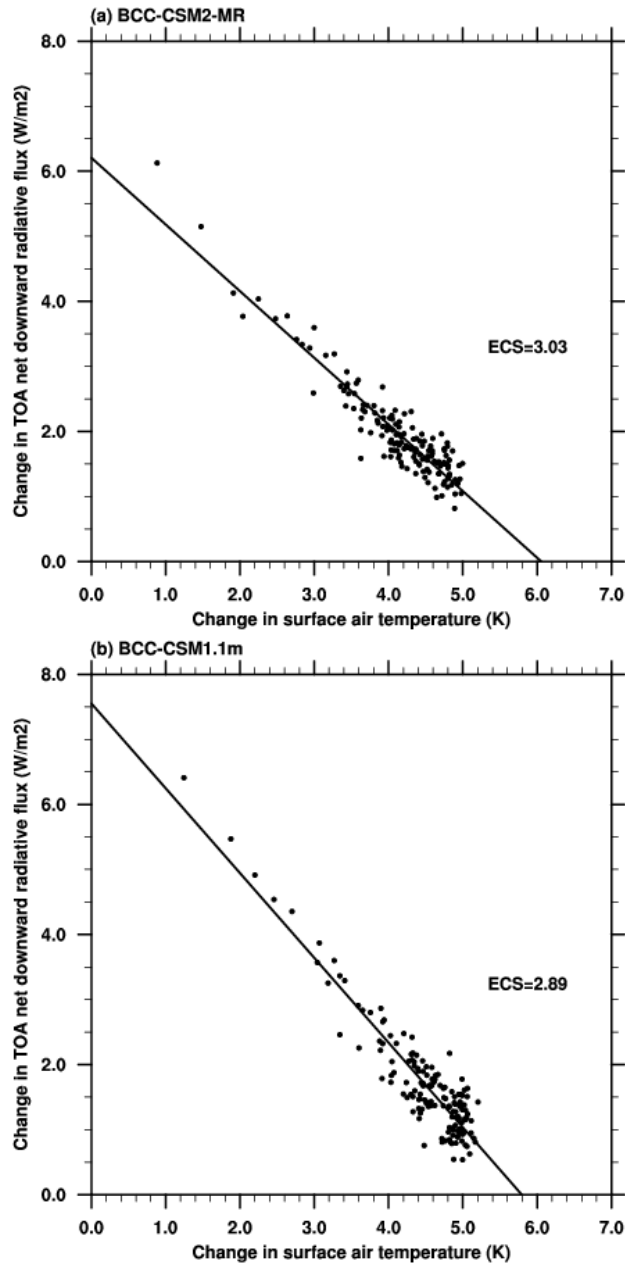


Figure 6. Relationships between the change in net top-of-atmosphere radiative flux and global-mean surface air temperature change simulated with an abrupt 4xCO<sub>2</sub> increase relative to the pre-industrial control run.



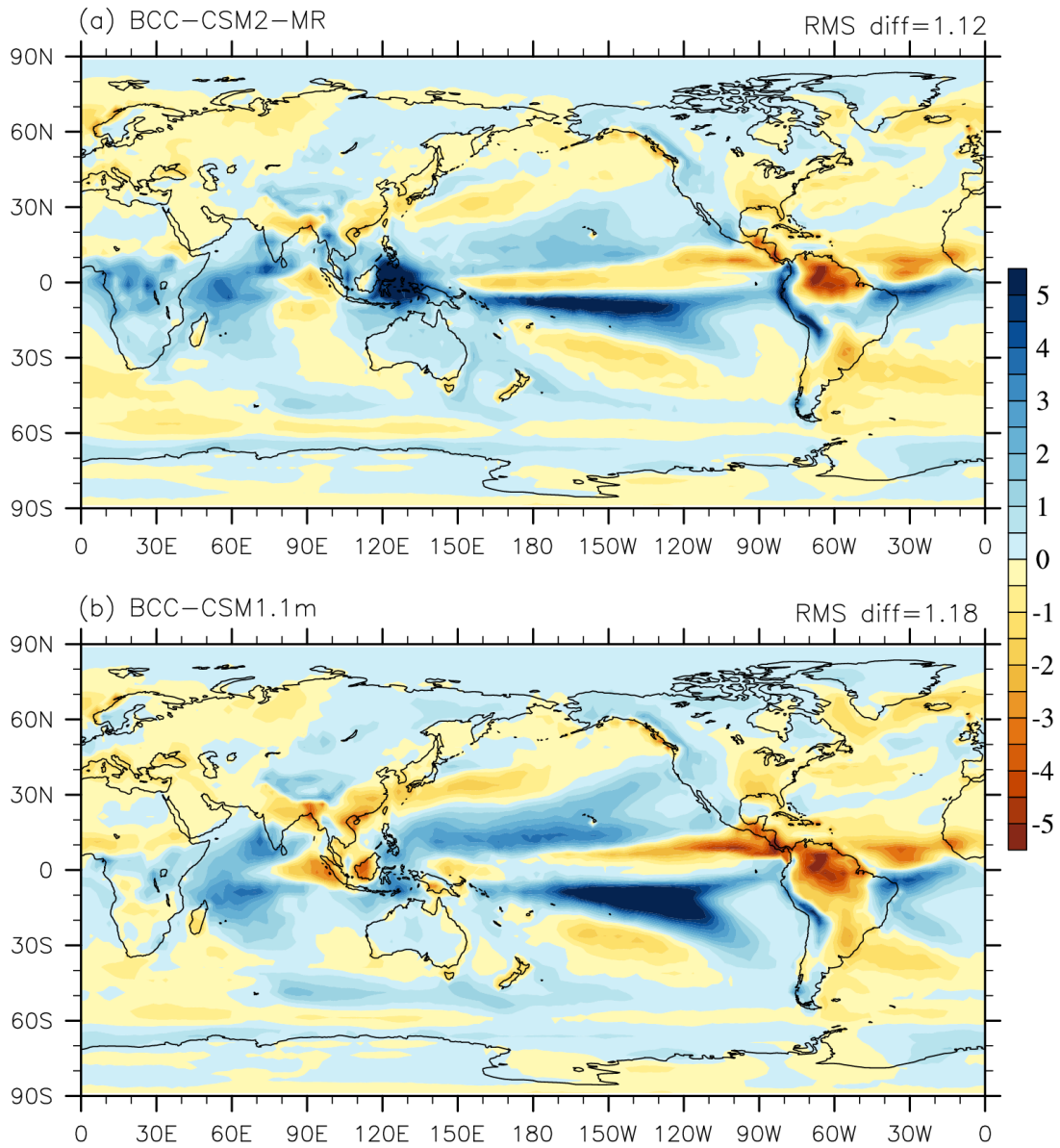


Figure 7. Annual-mean precipitation rate biases ( $\text{mm day}^{-1}$ ) of (a) BCC-CSM2-MR and (b) BCC-CSM1.1m simulations with contrast to 1986-2005 precipitation analyses from the Global Precipitation Climatology Project (Adler et al., 2003)

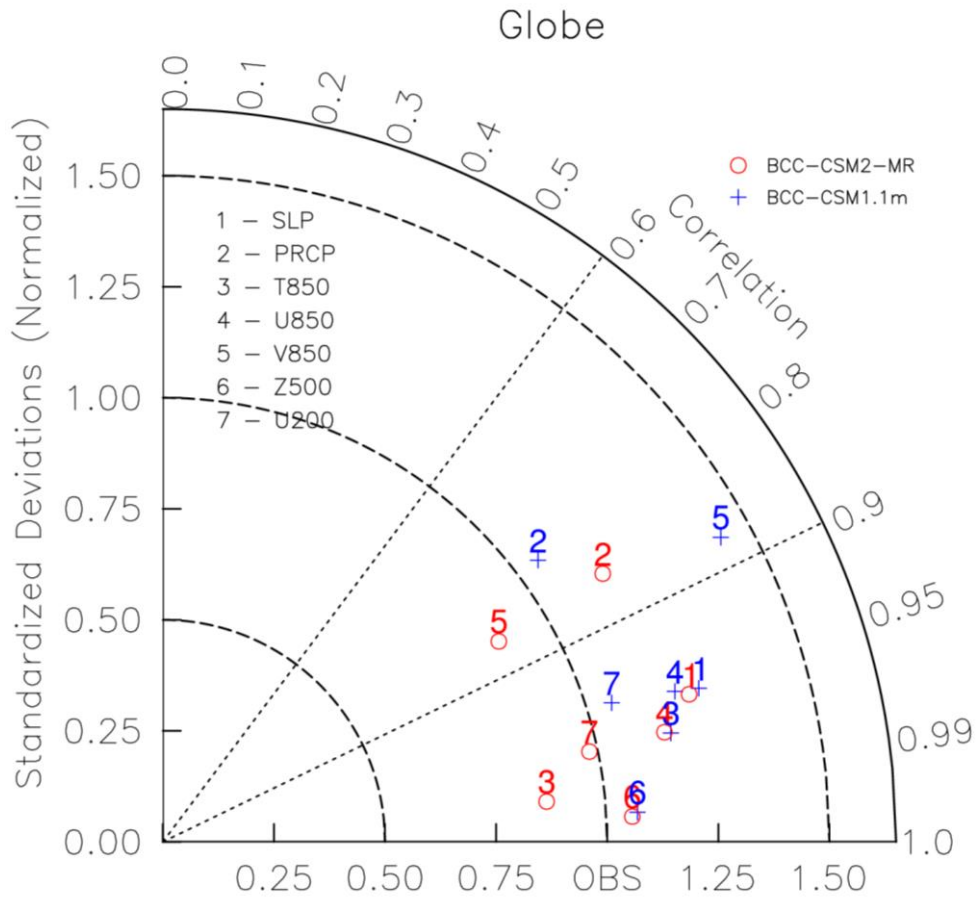


Figure 8. Taylor diagram for the global climatology (1980–2005) of sea level pressure (SLP), precipitation (PRCP), temperature at 850 hPa (T850), zonal wind at 850 hPa (U850), longitudinal wind at 850 hPa (V850), geopotential height at 500 hPa (Z500), and zonal wind at 200 hPa (U200). The radial coordinate shows the standard deviation of the spatial pattern, normalized by the observed standard deviation. The azimuthal variable shows the correlation of the modelled spatial pattern with the observed spatial pattern. Analysis is for the whole globe. The reference dataset is ERA-Interim except the precipitation from Global Precipitation Climatology Project dataset. The model results of BCC-CSM2-MR and BCC-CSM1.1m are the mean for 1980 to 2000. Blue crosses are for BCC-CSM1.1m and circles for BCC-CSM2-MR.

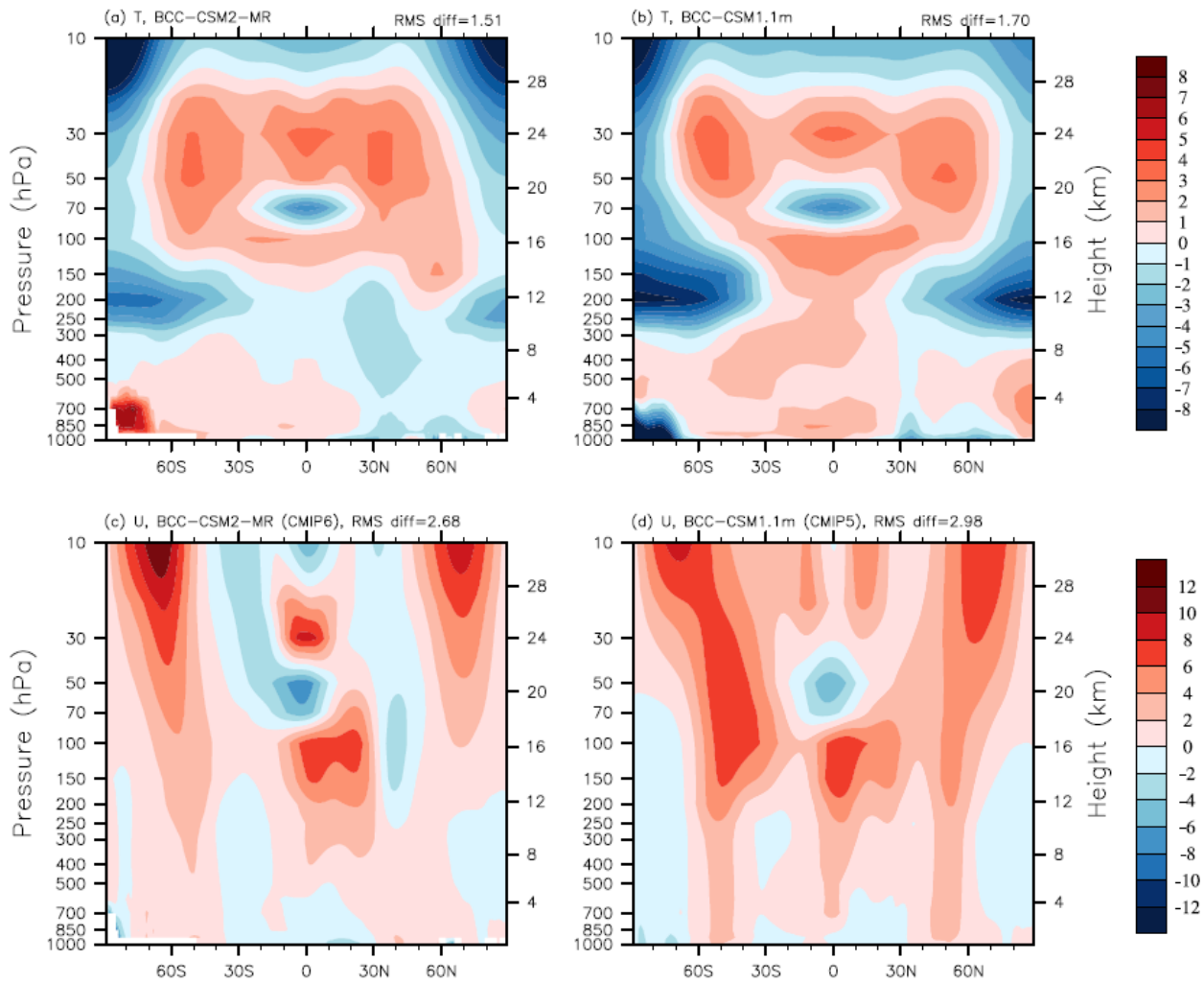


Figure 9. Pressure-latitude sections of annual mean temperature (top panels, K) and zonal wind (bottom, m s<sup>-1</sup>) biases for BCC-CSM2-MR (left) and BCC-CSM1.1m (right), with respect to the reanalysis ERA-Interim for the period of 1986 to 2005.

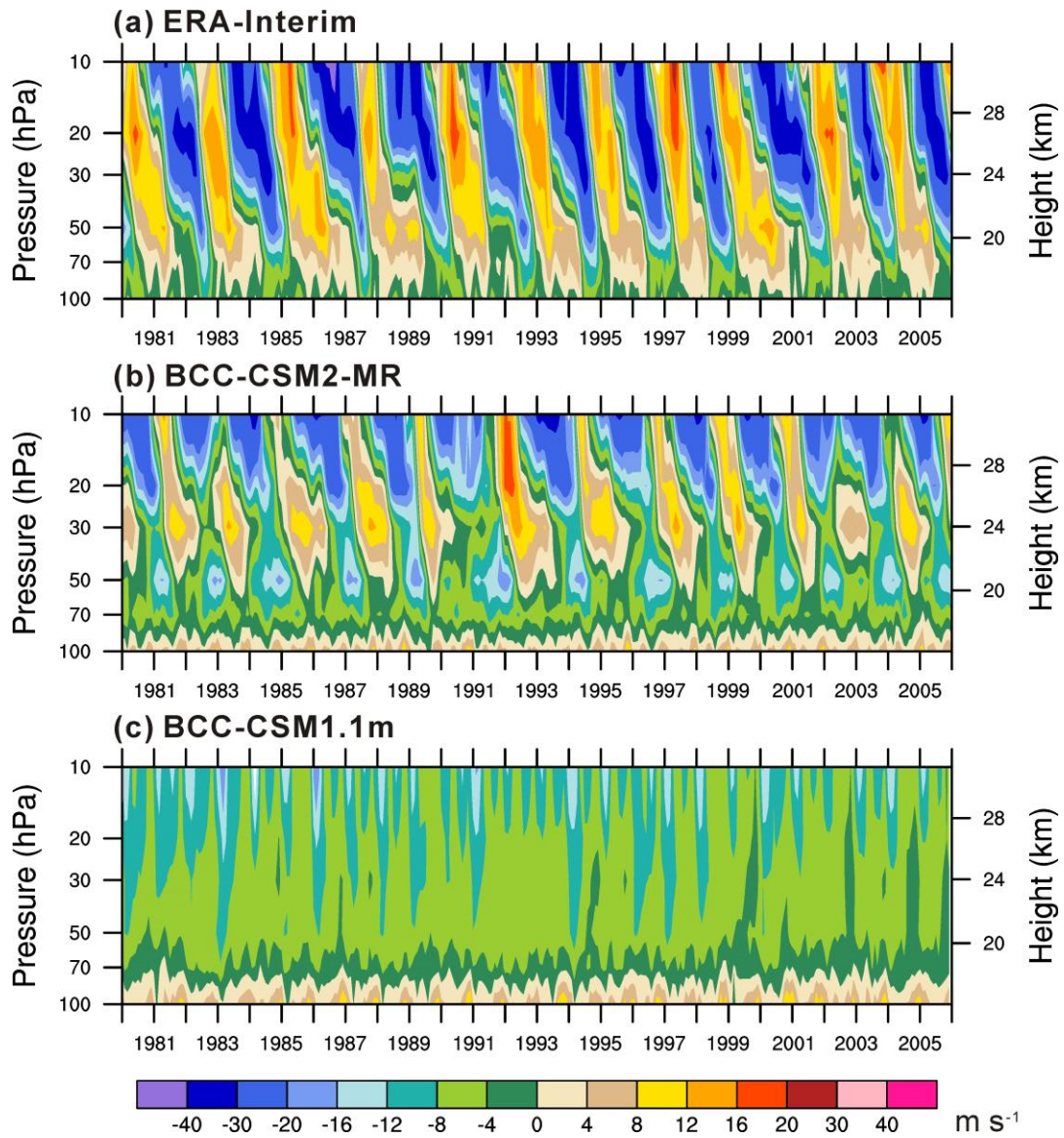


Figure 10. Tropical zonal winds ( $\text{m s}^{-1}$ ) between  $5^{\circ}\text{S}$  and  $5^{\circ}\text{N}$  in the lower stratosphere from 1980 to 2005 for (a) ERA-Interim reanalysis, (b) BCC-CSM2-MR, and (c) BCC-CSM1.1m.

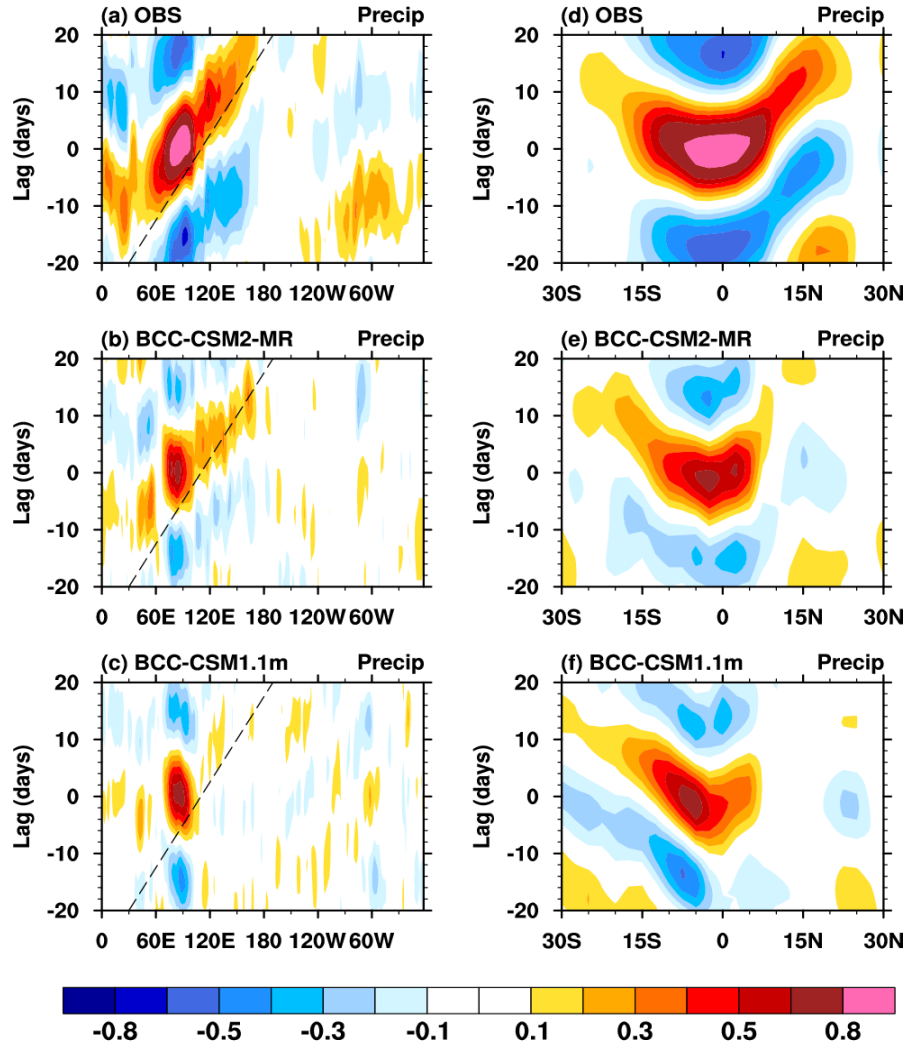


Figure 11. Left panels: longitude-time evolution of lagged correlation coefficient for the 20–100 day band-pass-filtered anomalous rainfall (averaged over 10°S–10°N) against itself averaged over the equatorial eastern Indian Ocean (75°E–85°E; 5°S–5°N). Right panels: same as in the left panels but to show meridional propagation of the filtered rainfalls, and lagged correlation coefficient for anomalous rainfall (averaged over 80°–100°E) against the rainfall averaged over the same region of equatorial eastern Indian Ocean. Dashed lines in each panel denote the 5 m s<sup>-1</sup> eastward propagation speed. The reference GPCP observations and historical simulations of models are from the period of 1997–2005.

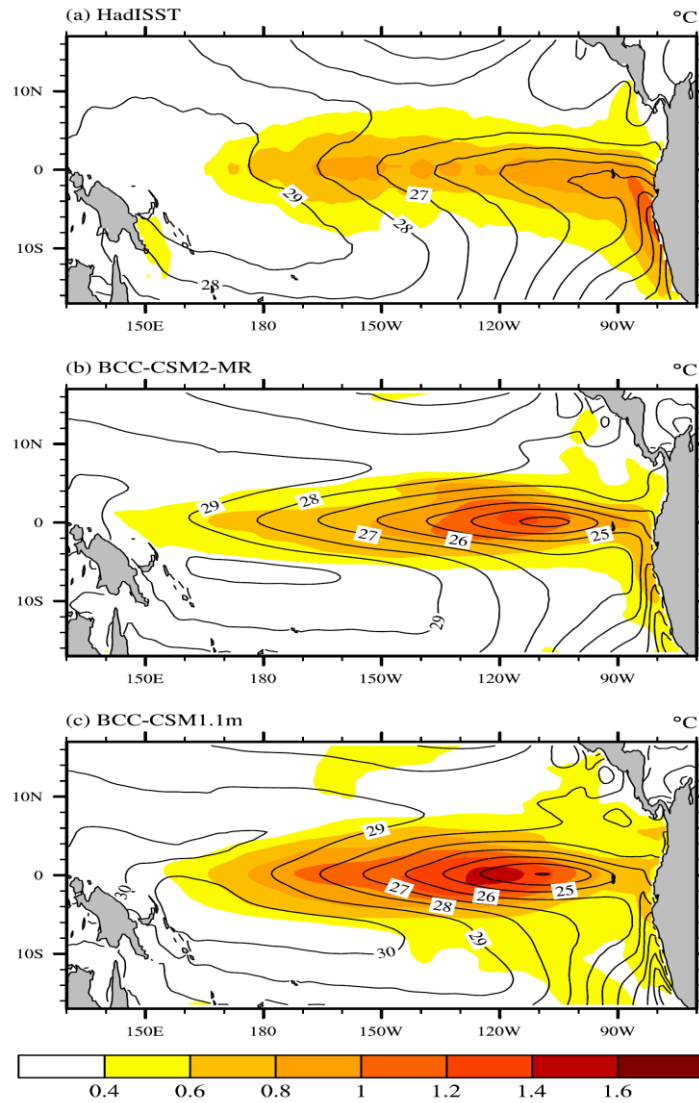


Figure 12. The spatial distributions of 1986-2005 annual mean sea surface temperature (contour lines, °C) and its standard deviation of interannual anomalies (shaded area, °C) in the tropical Pacific for (a) HadISST observations (Rayner et al., 2003), (b) BCC-CSM2-MR, (c) BCC-CSM1.1m.

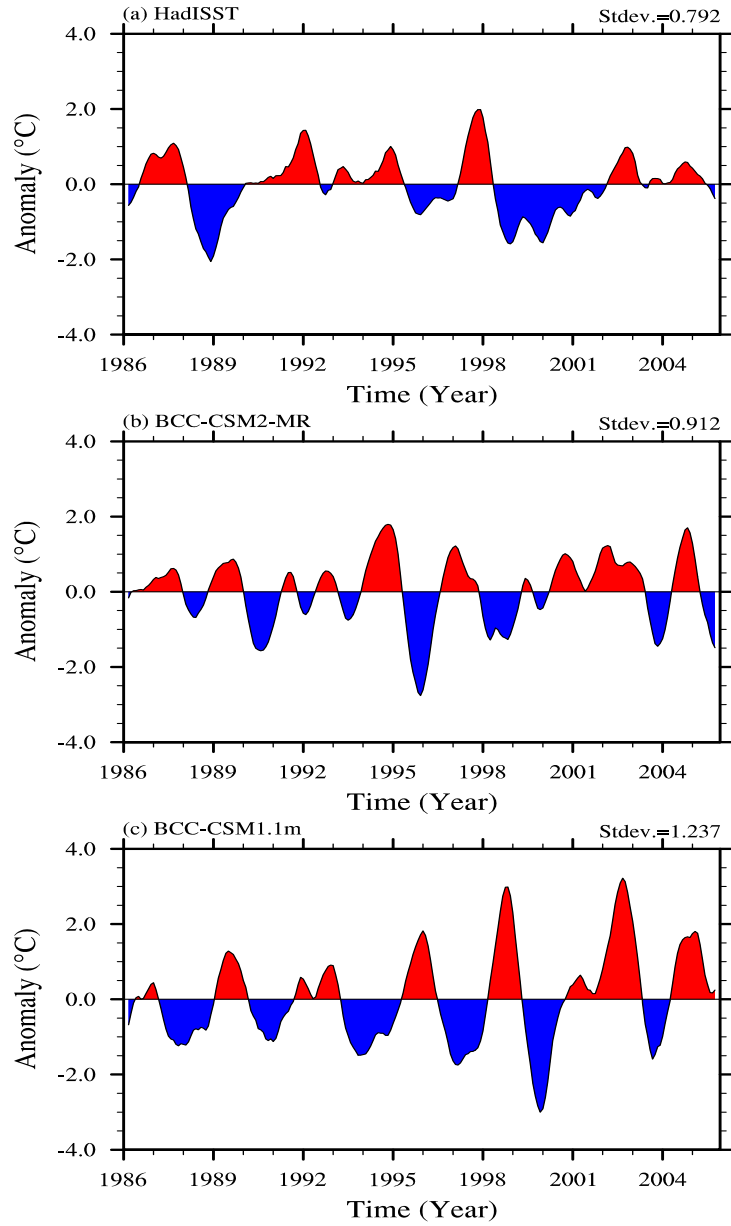


Figure 13. The time series of Niño3.4 SST Index from 1986 to 2005 for (a) HadISST data, (b) BCC-CSM2-MR, (c) BCC-CSM1.1m.

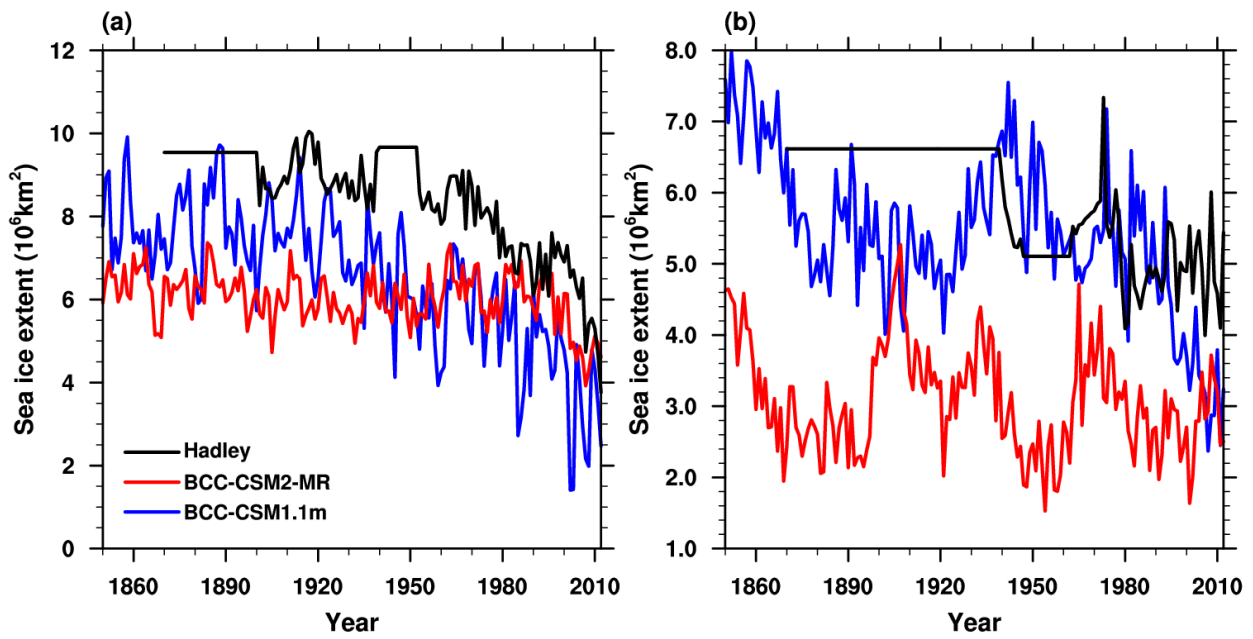


Figure 14. Time-series of sea-ice extent from 1851 to 2012 for (a) the Arctic in September and (b) the Antarctic in March as simulated in BCC-CSM2-MR and BCC-CSM1.1m and observations that are derived from Hadley Centre Sea Ice and Sea Surface Temperature data set (Rayner et al., 2003).



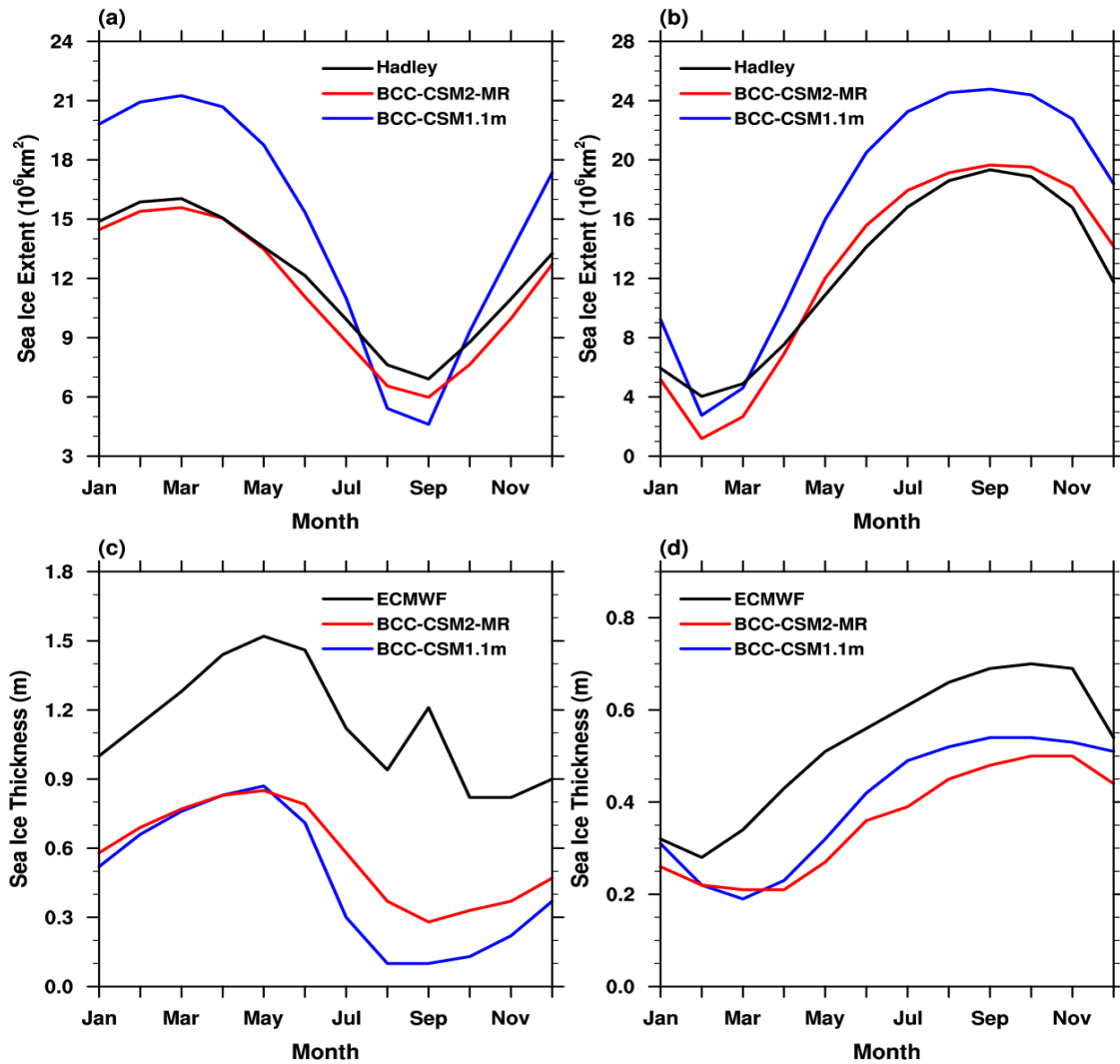


Figure 15. Mean (1980–2005) seasonal cycle of sea-ice extent (upper panel, the ocean area with a sea-ice concentration of at least 15%) and mean thickness (lower panel) in the Northern Hemisphere (left) and the Southern Hemisphere (right). The observed seasonal cycles of sea-ice extent in (a) and (b) are derived from 1980-2005 Hadley Centre Sea Ice and Sea Surface Temperature data set (Rayner et al., 2003), and the ice thickness in (c) and (d) are derived from 1980-2005 global gridded data set based on European Center for Medium-Range Weather Forecast (Tietsche, et al., 2014).

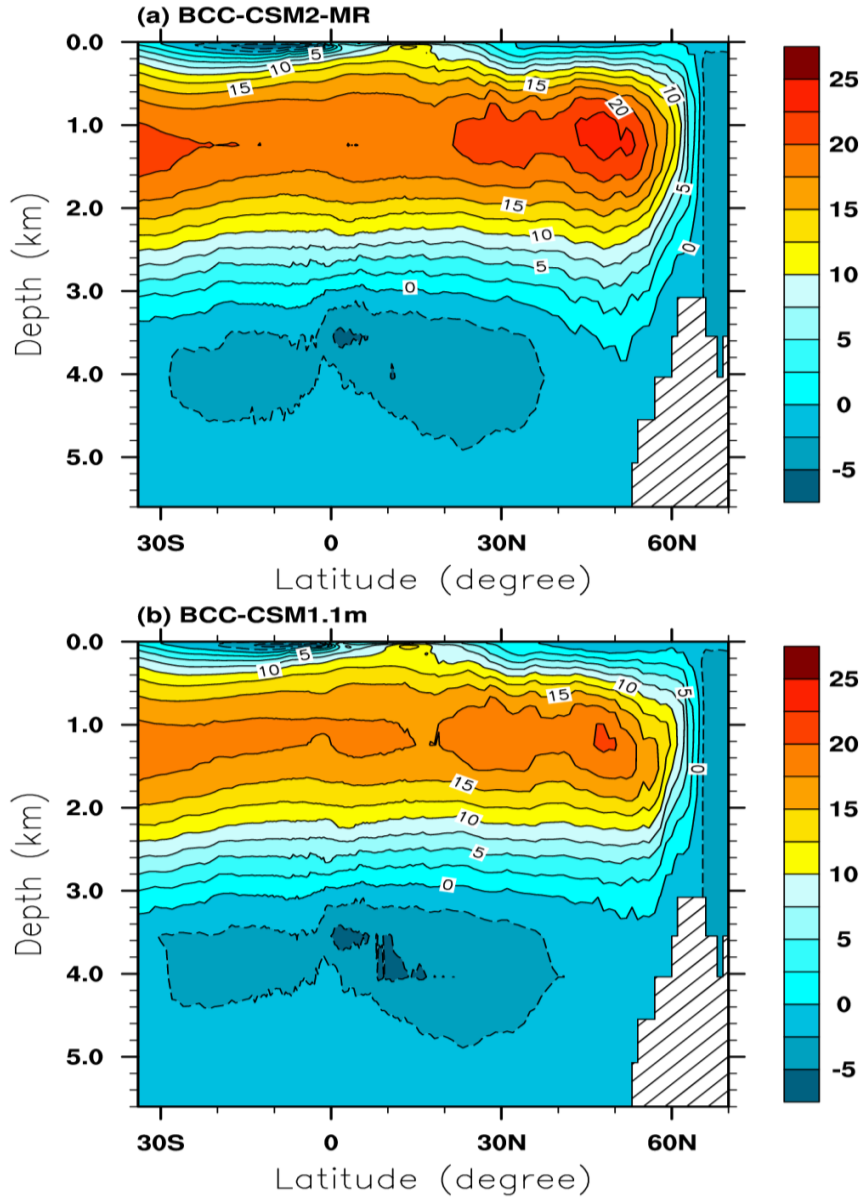


Figure 16. Zonally-averaged streamfunction of the Atlantic Meridional Overturning Circulation (AMOC) for the period of 1980 to 2005 in BCC-CSM2-MR (top) and BCC-CSM1.1m (bottom). Units: Sv

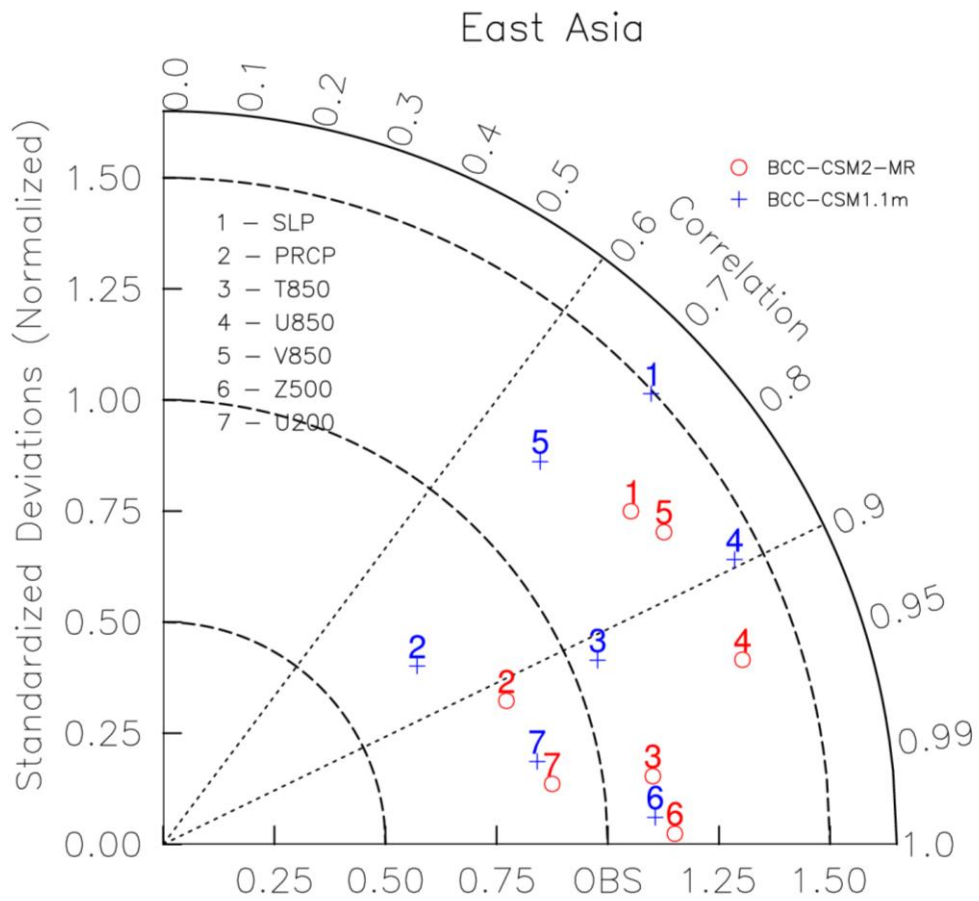


Figure 17. Same as in Figure 8, but for the domain covering East Asia (20°-50°N, 100°-140°E).

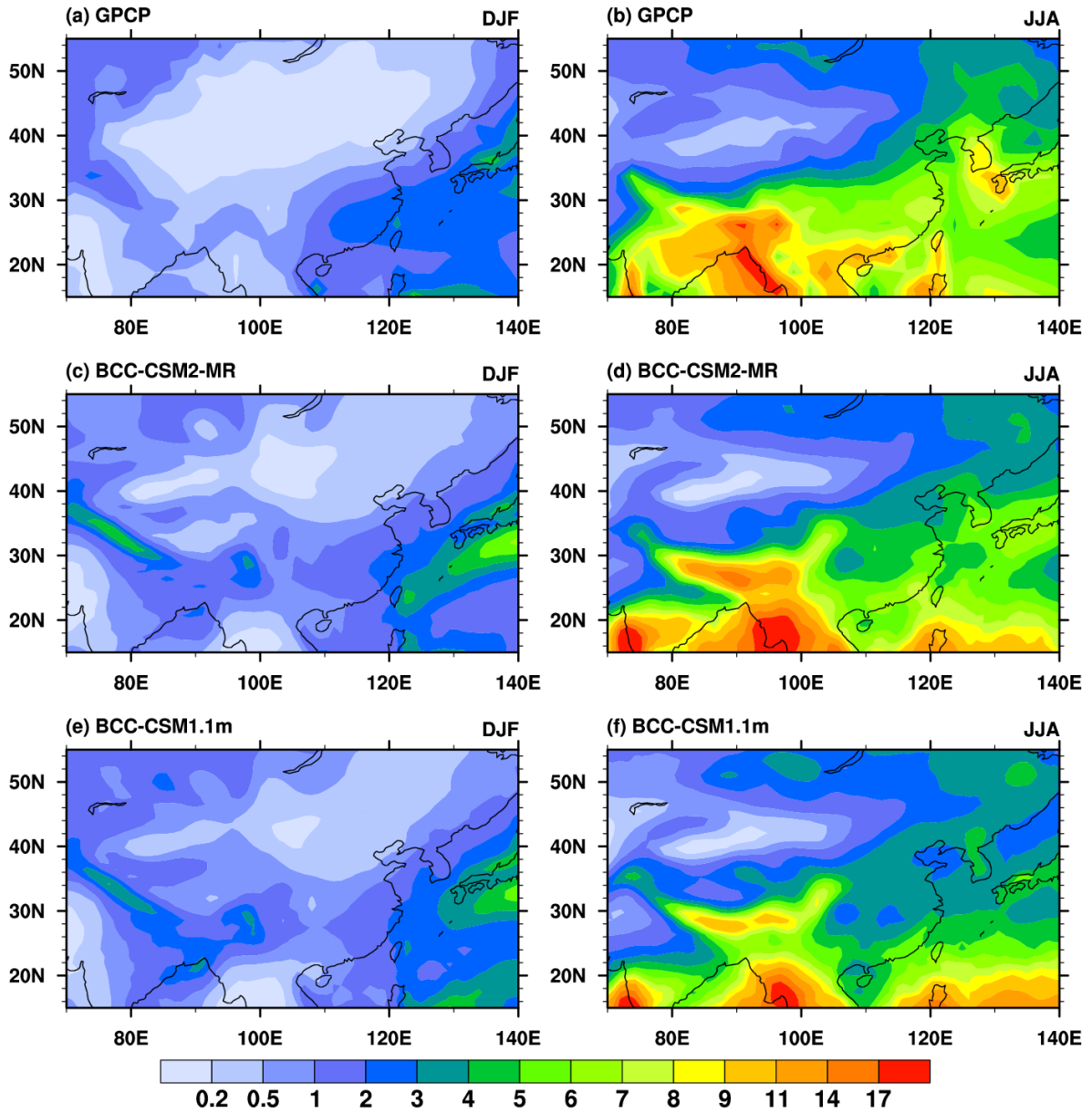


Figure 18. Regional distribution maps of precipitation climatology (averaged from 1980 to 2005) for December-January-February (left panels) and June-July-August (right panels) from (a) GPCP, (b) BCC-CSM2-MR, (c) BCC-CSM1.1m. Units:  $\text{mm day}^{-1}$ .

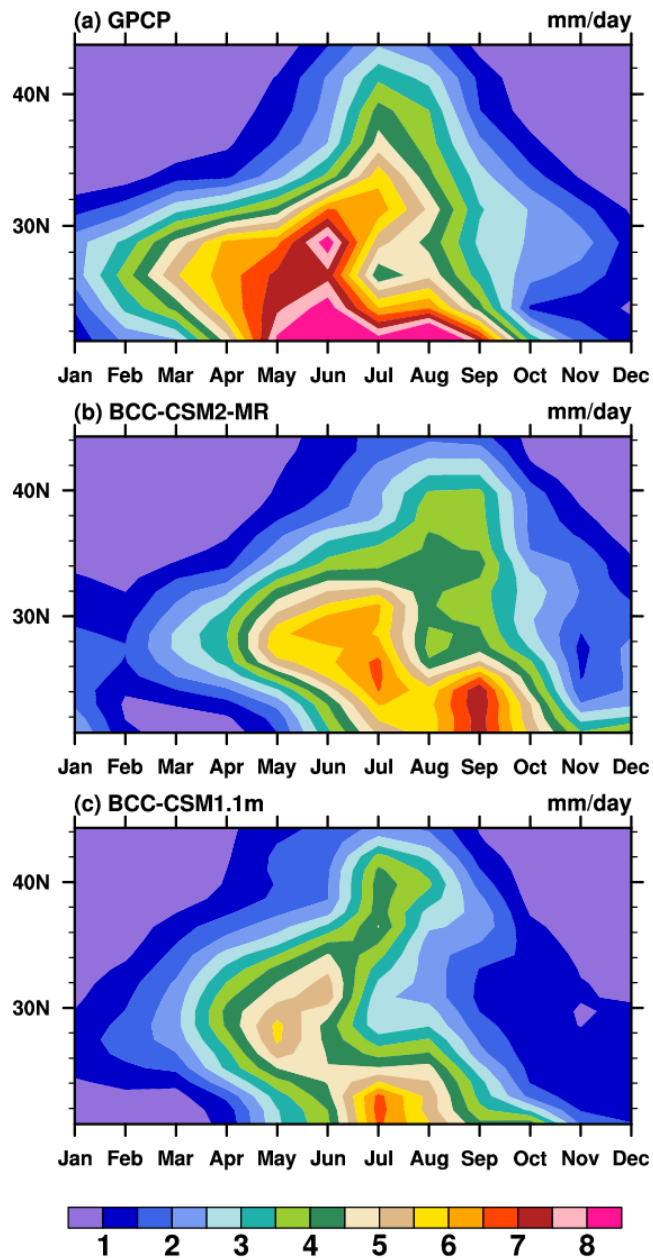


Figure 19. Latitude (from 20°N to 25°N) – month (Jan. to Dec.) diagrams showing variations of monthly precipitation averaged over 100°E–120°E and for the period of 1980–2005. (a) GPCP, (b) BCC-CSM2-MR, (c) BCC-CSM1.1m. Units: mm day<sup>-1</sup>.

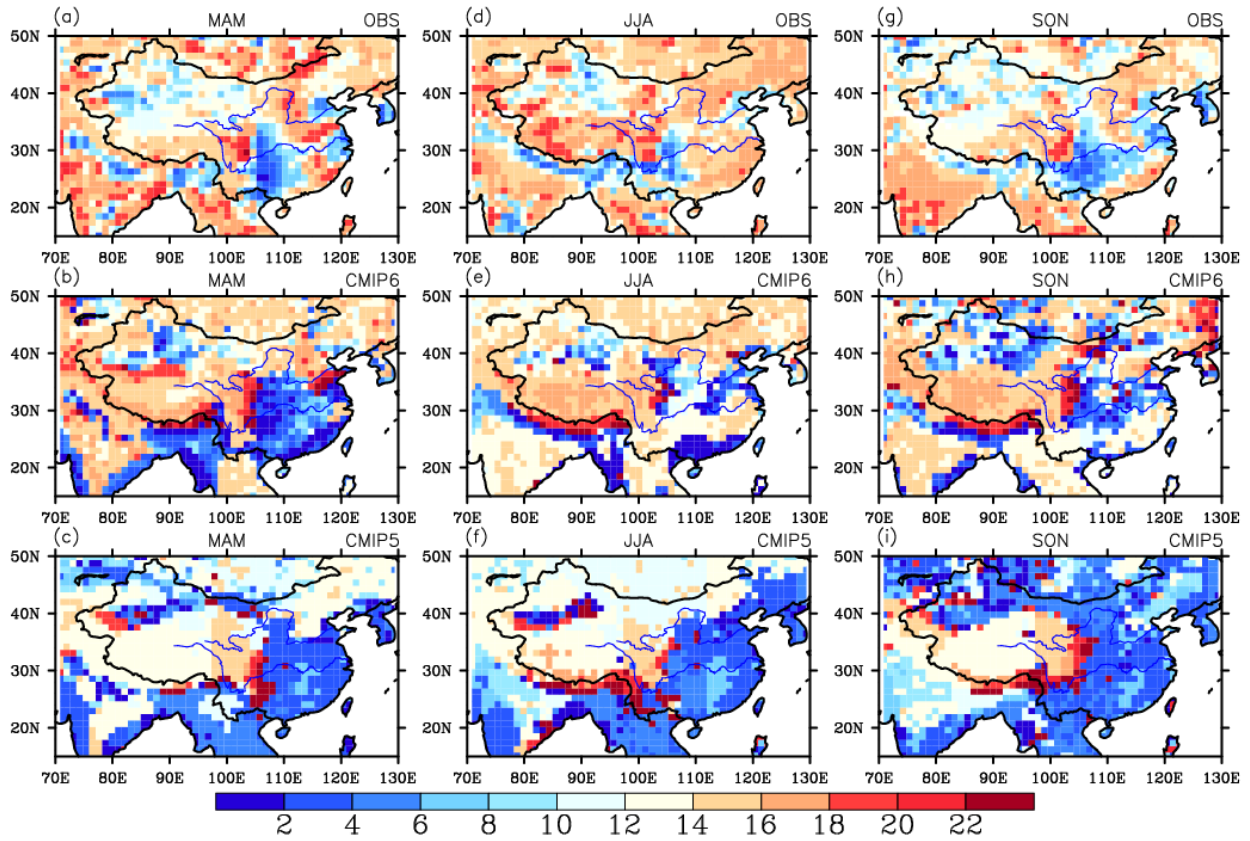


Figure 20. Local times of maximum frequency of rainfall occurrence in March-April-May (left column), June-July-August (middle column), and September-October-November (right column) over China and its surrounding areas for BCC-CSM2-MR (middle panel), BCC-CSM1.1m (bottom panel), and TRMM data (top panel, Huffman et al., 2014). The rainfall occurrence is defined as the hourly precipitation larger than 1 mm.